ACCSCIENCE PUBLISHING

Engineering Science in Additive Manufacturing

ORIGINAL RESEARCH ARTICLE

Regulation mechanism of heat input on *in situ* tempering and precipitation behavior of wire arc additively manufactured 1,600 MPa low-alloy ultra-high-strength steel

Kun Li[1,2,3], Shuang Jun Zhang[1,3], Ziche Li[1,3,4], Shixin Xu[5], Xuru Hou[4], Peng Li[6], Xiangrui Wan[5], Liang Zhu[1,3]*, Chen Ji[1,3], Yang Cao[4], Lin Zhao[4]*, Chengyong Ma[4], and Zhiling Tian[4,7]

[1]State Key Laboratory of Mechanical Transmission for Advanced Equipment, College of Mechanical and Vehicle Engineering, Chongqing University, Chongqing, China

[2]Department of Advanced Interdisciplinary Manufacturing, Institute of Advanced Interdisciplinary Studies, Chongqing University, Chongqing, China

[3]Chongqing Key Laboratory of High-performance Structural Additive Manufacturing, College of Mechanical and Vehicle Engineering, Chongqing University, Chongqing, China

[4]Department of Metal Materials Research, Central Iron and Steel Research Institute Group, Beijing, China

[5]CISDI Research & Development Co., Ltd., Chongqing, China

[6]Department of Additive Manufacturing Materials, MCC Kunyuan (Chongqing) Metal Materials Research Institute Co., Ltd., Chongqing, China

[7]The Chinese Society for Metals, Beijing, China

***Corresponding authors:**
Liang Zhu
(zhuliang@cqu.edu.cn);
Lin Zhao
(hhnds@aliyun.com)

Citation: Li K, Zhang SJ, Li Z, *et al*. Regulation mechanism of heat input on *in situ* tempering and precipitation behavior of wire arc additively manufactured 1,600 MPa low-alloy ultra-high-strength steel. *Eng Sci Add Manuf*. 2026;2(4):026370021. doi: 10.36922/ESAM026370021

Received: September 7, 2026

Revised: September 23, 2026

Accepted: October 8, 2026

Published online: October 22, 2026

Copyright: © 2026 Author(s). This is an Open-Access article distributed under the terms of the Creative Commons Attribution License, permitting distribution, and reproduction in any medium, provided the original work is properly cited.

Publisher's Note: AccScience Publishing remains neutral with regard to jurisdictional claims in published maps and institutional affiliations.

Abstract

With surging demand for lightweight, high-strength metal components in high-end equipment and large-scale engineering structures, additive manufacturing of low-alloy ultra-high-strength steel (LUHSS) has become a hot research topic. Wire arc additive manufacturing (WAAM) shows remarkable potential for fabricating large LUHSS components; however, repetitive thermal cycles can trigger *in situ* tempering, significantly affecting carbide evolution and mechanical properties. To address this, this study employed a cold metal transfer plus pulse (CMT+P)-based WAAM process to fabricate thin-walled LUHSS specimens under gradient heat input conditions (3.73, 7.37, and 11.8 kJ/cm) and systematically characterized their mechanical properties and microstructure. The results indicate that increasing heat input enlarges the melt pool and weld bead dimensions, while excessive heat input exacerbates oxide inclusion precipitation and compromises forming quality; the deposited microstructure consists primarily of lamellar martensite, retained austenite, and dispersed carbides. Heat input can precisely control the *in situ* tempering effect, driving the gradual transformation of carbides from pure $Cr_{23}C_6$ to a coexistence of $Cr_{23}C_6$ and Cr_3C, ultimately forming Cr_7C_3. Grain coarsening and dislocation recovery weaken the material's strengthening effect. At a heat input of 3.73 kJ/cm, the specimen exhibited excellent strength–ductility synergy and near-isotropic characteristics, with tensile strength, yield strength, and elongation of 1,529 MPa, 1,272 MPa, and 12.3%, respectively. This study shows how heat input-induced *in situ* tempering regulates precipitation behavior and the mechanical properties of WAAM-formed LUHSS.

Keywords: Wire arc additive manufacturing; Low-alloy ultra-high-strength steel; Heat input; Microstructure evolution

1. Introduction

Low-alloy ultra-high-strength steel (LUHSS) offers excellent mechanical properties, good weldability, and strong engineering economics, making it widely used in critical fields such as defense equipment, high-end transportation, and offshore engineering.[1-3] However, traditional forming processes such as casting, forging, and machining struggle to efficiently and precisely fabricate large-sized, complex-geometry LUHSS components. Traditional processing methods generally suffer from high forming loads, primary solidification defects (in castings and forging blanks), and limited forming flexibility, which severely hinder the engineering adoption and large-scale industrial application of LUHSS[4]. Wire arc additive manufacturing (WAAM), with its unique process advantages—including high deposition efficiency, low production costs, short production cycles, and no constraints on part dimensions—offers an efficient and reliable technical solution for overcoming the bottlenecks of traditional LUHSS manufacturing.[5,6] Combined with the excellent welding and forming properties of LUHSS, WAAM shows tremendous application potential and promising prospects for integrated, monolithic, near-net-shape manufacturing of large-scale ultra-high-strength steel structural components[7].

Although WAAM technology offers significant process advantages for the integrated fabrication of LUHSS components, its layer-by-layer deposition process introduces complex transient thermal behavior, which directly determines the dimensional accuracy, surface quality, and stability of the mechanical properties of the deposited components[8]. Therefore, precise thermal management throughout the entire process is a key prerequisite for achieving high-performance, highly reliable LUHSS components via WAAM. To address forming defects and performance fluctuations in different alloy systems, effective control can be achieved through process parameter optimization and active thermal control strategies. At this stage, mainstream control methods include heat input [9,10], wire feeding speed and travel speed [11,12], deposition paths and forming patterns [13], shielding gas conditions [14,15], deposition strategy [16], and other key process parameters. At the same time, auxiliary thermal control can be achieved by adjusting the interlayer temperature and interlayer dwell time.[17,18] Among the numerous control variables, heat input is a key parameter that determines forming quality; it directly governs thermal cycling characteristics, cooling rates, the dynamic behavior of the molten pool, and *in situ* heat-treatment effects in the WAAM forming process. From the perspective of the forming mechanism itself, heat input profoundly regulates the solidification behavior of the deposited metal, the solid-state phase transformation pathways, and the evolution of nano-precipitates, ultimately determining the microstructure and macroscopic mechanical properties of LUHSS components formed via WAAM.[19-23]

Domestic and international research on WAAM-formed low-alloy high-strength (HSLA) steel has confirmed the decisive role of heat input in determining microstructure and mechanical properties; however, conclusions in existing studies remain highly controversial. Yildiz *et al.*[24] showed that low heat input promotes martensitic transformation in ER120S-G steel produced by WAAM, increasing strength, whereas excessively high heat input induces ferrite precipitation, degrading the material's strength. Fang *et al.*[25], in their study of WAAM in 800 MPa-grade high-strength steel, similarly confirmed that increased heat input promotes a microstructural transformation from lamellar martensite/baithite to granular baithite, leading to a decline in mechanical properties. However, contradictory conclusions have also been reported. Rodrigues *et al.*[26] and Duarte *et al.*[27] observed that higher heat input could simultaneously improve strength and ductility in WAAM-ed ER110S-G steel. The conflicting findings indicate that the mechanisms by which heat input modulates steel's mechanical properties are strongly alloy-dependent and closely coupled with the microstructural evolution induced by thermal cycling.

Compared with conventional HSLA steel, LUHSS has a higher strength grade and a distinct mechanism for strength and toughness enhancement; the two differ fundamentally in microstructural response and performance evolution patterns. The strength and toughness enhancement mechanism of conventional HSLA steel primarily relies on the synergistic effects of grain refinement, solid solution strengthening, and precipitation strengthening[28], whereas the performance improvement of LUHSS is mainly attributed to the coupled regulation of multiple mechanisms, including grain refinement, dislocation strengthening, and precipitation strengthening[29]. More importantly, the martensitic matrix and carbide precipitation behavior of LUHSS are highly sensitive to the alternating and complex thermal cycles involved in WAAM layer-by-layer deposition. Repeated thermal exposure during layer-by-layer deposition can significantly alter carbide precipitation and evolution, thereby reshaping the material's strengthening mechanisms and modulating its macroscopic mechanical properties. This type of *in situ* tempering phenomenon induced by cyclic reheating has been preliminarily confirmed in research on the additive manufacturing of martensitic steels.[30,31] Existing research has largely focused on macroscopic microstructural

observations and has not elucidated the coupling among heat input, precipitated phases, *in situ* tempering, and high ductility; furthermore, it lacks a systematic analysis of carbide evolution patterns. Investigating the mechanisms governing heat input is central to producing high-performance LUHSS via WAAM.

Herein, this study employs cold metal transfer coupled pulse arc additive manufacturing (CMT+P-WAAM) technology to fabricate thin-walled LUHSS specimens under three sets of graded heat input conditions—3.73 kJ/cm, 7.37 kJ/cm, and 11.8 kJ/cm—with a focus on investigating the heat input-induced *in situ* tempering mechanism triggered by layer-by-layer alternating thermal cycles. This systematic investigation examines how heat input influences microstructural evolution, carbide precipitation behavior, multiscale strengthening mechanisms, and mechanical properties in LUHSS, elucidating the intrinsic relationship between carbide evolution characteristics, martensitic microstructural stability, and the synergistic response of strength and ductility. This study also establishes a structure–property relationship between the microstructure and macroscopic properties of WAAM-ed LUHSS, and provides a theoretical basis and technical support for process optimization and precise performance control in the arc additive manufacturing of ultra-high-strength steel.

2. Materials and methods

2.1. Materials

A 1.2 mm-diameter wire of 1,600 MPa-grade LUHSS was adopted as the feedstock material, while a 316 stainless steel plate with dimensions of 650 mm × 155 mm × 20 mm served as the substrate. The chemical compositions of the welding wire and substrate are summarized in Table 1. Prior to the deposition experiments, surface rust on the substrate was removed via abrasive grinding with an angle grinder, followed by ultrasonic cleaning using acetone to thoroughly eliminate surface grease and contaminants.

2.2. Cold metal transfer coupled pulse-based wire arc additive manufacturing system

The complete CMT+P-WAAM platform and the adopted deposition scanning strategy are presented in Figure 1a. The overall experimental setup comprises three core subsystems: a Fronius (Austria) welding unit, a six-axis ABB (China) robotic manipulator, and an upper-computer control system. The Fronius welding subsystem included a CMT Advanced 4,000 R welding power source, a VR1550 4R/F++ robotic wire feeder, a 4,000-R FC cooling circulation tank, and an independent shielding gas supply unit. A NAC Memrecam HX-5E high-speed camera (NAC Image Technology Inc., Japan) operating at a frame rate of 5,000 fps was deployed to capture the transient dynamic evolution of the molten pool in real time. A German AH-XXV-2E Hannover online welding monitor was electrically linked to the welding torch and workbench to synchronously record instantaneous welding current and voltage signals during single-bead deposition, enabling quantitative evaluation of arc stability throughout the forming process. An S-shaped reciprocating scanning path was adopted to fabricate thin-walled LUHSS specimens for satisfactory forming integrity. The interlayer temperature was strictly maintained below 120°C to avoid bead sagging and collapse induced by accumulated thermal energy. Additional fixed process parameters were defined as follows: the wire stick-out length was set to 15 mm, and high-purity argon (99.99 vol.%) was applied as the protective shielding gas at a constant flow rate of 20 L/min. All specimens were deposited under the CMT+P arc mode. The heat input generated during WAAM deposition was calculated using the standard welding heat input formula (**Equation 1**). The process parameters are shown in **Table 2**.

$$E = \frac{I \times U}{100v} \tag{1}$$

where I is the welding current (A), U is the welding voltage (V), and v is the travel speed.

2.3. Microhardness characterization and phase analysis

Metallographic, microhardness, and tensile samples were obtained using electrical discharge machining and machining at the sampling locations shown in Figure 1b. The metallographic sample size was 10 × 10 × 5 mm. After grinding and polishing, the metallographic samples were corroded with a 10% nitric acid alcohol solution by

Table 1. Chemical composition of the wire and substrate in wt.%

Material	Carbon	Silicon	Manganese	Chromium	Nickel	Molybdenum	Tungsten	Vanadium	Ferum
Wire	0.30	0.93	0.77	3.14	1.09	0.75	1.02	0.19	Balance
Base metal	≤0.03	≤1.00	≤2.0	16.0~18.5	12.0~17.0	2.0~3.0	–	–	Balance

Table 2. Wire arc additive manufacturing heat input process parameters

Sample	Wire feed speed	Travel speed	Welding voltage	Welding current	Heat input
Low	5 m/min	7 mm/s	17.4 V	150 A	3.73 kJ/cm
Middle	8 m/min	6 mm/s	20.1 V	220 A	7.37 kJ/cm
High	11 m/min	5 mm/s	21.1 V	280 A	11.8 kJ/cm

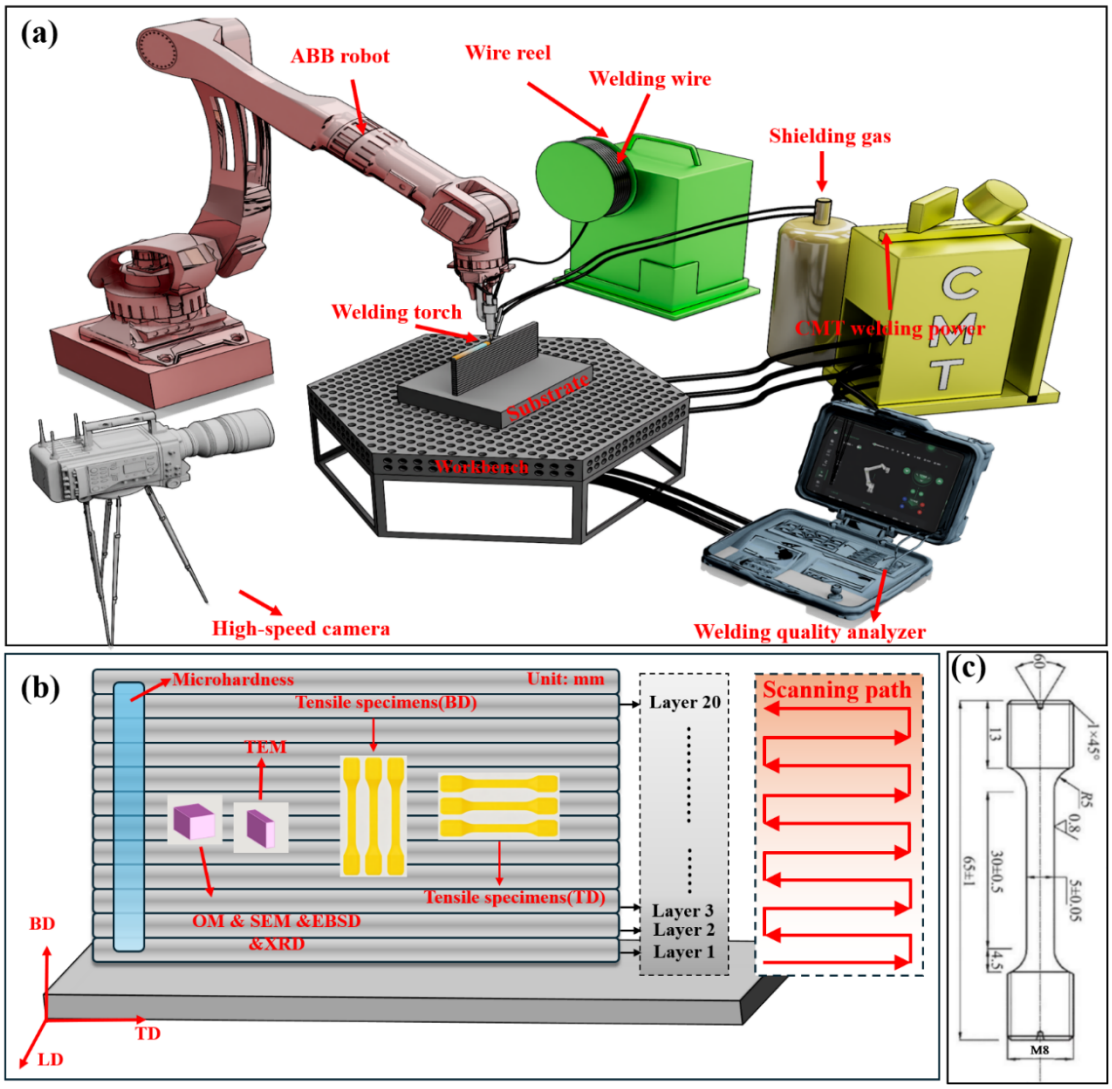


Figure 1. Overview of the pulse-cold metal transfer wire arc additive manufacturing setup, specimen sampling scheme and tensile sample dimensions. (a) Cold metal transfer coupled pulse-based wire arc additive manufacturing system, (b) schematic of metallography and mechanical properties specimens sampling location and deposition strategy, (c) tensile specimen dimensions.

volume for 15 to 20 seconds. The microstructure of the metallographic samples was observed using the OLYMPUS GX53 optical microscope (OM; Olympus, Japan) and the Quanta650 field-emission scanning electron microscope (SEM; Phenom ProX, Netherlands). Oxide inclusions were statistically analyzed using ImageJ software (version 6). For each heat-input condition, at least 10 representative micrographs were analyzed. Consistent image-processing and particle-analysis settings were applied to determine the inclusion size distribution and area fraction.

Phase analysis was performed using X-ray diffraction (XRD; AL2700B, Shandong Aolongrui Instrument Co., Ltd., China), with a cobalt target. The measurement angle range was 20° to 110°, and the scanning rate was 2°/min; the experimental data were analyzed using Jade 6.5 software. The grains and texture of the material were characterized using electron backscatter diffraction (EBSD; Symmetry S3, Oxford Instruments, United Kingdom), and the experimental data were analyzed using AZtecCrystal software (version 2.1). The fine structure and nano-precipitates were characterized using an FEI Tecnai G2 F20 transmission electron microscope (TEM; FEI, United States), and the chemical composition of the nano-precipitates was determined using the energy-dispersive spectrometer (EDS; Phenom ProX, Netherlands) equipped in the TEM. High-resolution TEM (HRTEM; HF5000, Hitachi High-Tech, Japan) was also used to characterize the precipitates.

Fast Fourier transform (FFT) analysis of HRTEM images was performed using DigitalMicrograph software to identify the crystal structure of precipitates. The continuous cooling transformation curve of the LUHSS was calculated by JMatPro software (version 13.2, Sente Software, United Kingdom). The chemical composition of the welding wire, grain size, and austenitizing temperature were imported as input parameters. The resulting continuous cooling transformation diagram was used to assess the occurrence of diffusion-type phase transformations (bainite and pearlite) at the three actual cooling rates used in this experiment.

2.4. Mechanical testing

Room-temperature tensile tests were implemented on an ETM-105D universal testing machine (ETM-105D, Wance, China) at a constant crosshead speed of 2 mm/min in compliance with the Chinese standard GB/T 228.1-2021; tensile specimens were extracted along both the transverse direction (TD) and building direction (BD), and their geometric dimensions are displayed in Figure 1c. All tensile property data were averaged from three parallel replicates to guarantee statistical validity, and SEM was adopted to characterize the fracture morphologies of broken tensile samples. Vickers microhardness measurements along the BD with an indentation spacing of 2.5 mm were performed via a VH-5 digital hardness tester (VH-5, Shanghai Yanrun Optical Machinery Technology Co., Ltd., China) under an applied load of 3,000 gf and a dwell time of 15 seconds, while inductively coupled plasma optical emission spectrometry (Plasma 3000; NCS Testing Technology Co., Ltd., China) was utilized to measure the elemental compositions of the original welding wire and WAAM-ed alloy.

3. Results and discussion

3.1. Evaluation of heat input on deposition process and bead characteristics

Single-track single-layer deposition acted as the basic forming unit for WAAM-ed thin-walled parts, and its process stability directly governed the overall forming performance of the as-deposited structures; the corresponding current–voltage waveforms recorded under varied heat input levels are presented in Figure 2. The CMT+P hybrid process integrates the low-heat input and spatter-free merits of conventional CMT technology alongside high deposition efficiency, which expands the adjustable heat input window, suppresses pore defects inside deposited layers, and improves the stability of the additive manufacturing process.[32] A complete CMT+P cycle comprises a pulse stage and a CMT short-circuit stage [33], and the total cycle duration rose progressively with elevated heat input, as illustrated in Figure 2a–c: the cycle length reached 71 ms at a heat input of 3.73 kJ/cm (containing seven pulse transitions and one CMT short-circuit transition), while it extended to 204 ms under the highest heat input of 11.8 kJ/cm (including 40 pulse transitions and one CMT transition). Furthermore, peak current, peak current holding duration, and pulse frequency all increased markedly with heat input, as summarized in Figure 2d.

The ratio of wire feeding speed to travelling speed is the key parameter for controlling heat input; increasing the wire feeding speed/travelling speed ratio leads to an increase in the characteristic dimensions of the bead.[24] As heat input increased, the molten pool size increased significantly (Figure 3a–c), resulting in a significant increase in the tail size of the weld bead (Figure 3d–f). Moreover, the bead width (B), bead height (H_1), bead penetration depth (H_2), and wetting angle (θ) all increased as heat input increased (Figure 3j). Arc force plays an important role in the deposition process of molten droplets.[34] The arc force increased with heat input, resulting in deeper bead penetration. Increasing the wire feeding speed will also lead to a greater arc deposition rate, which can be

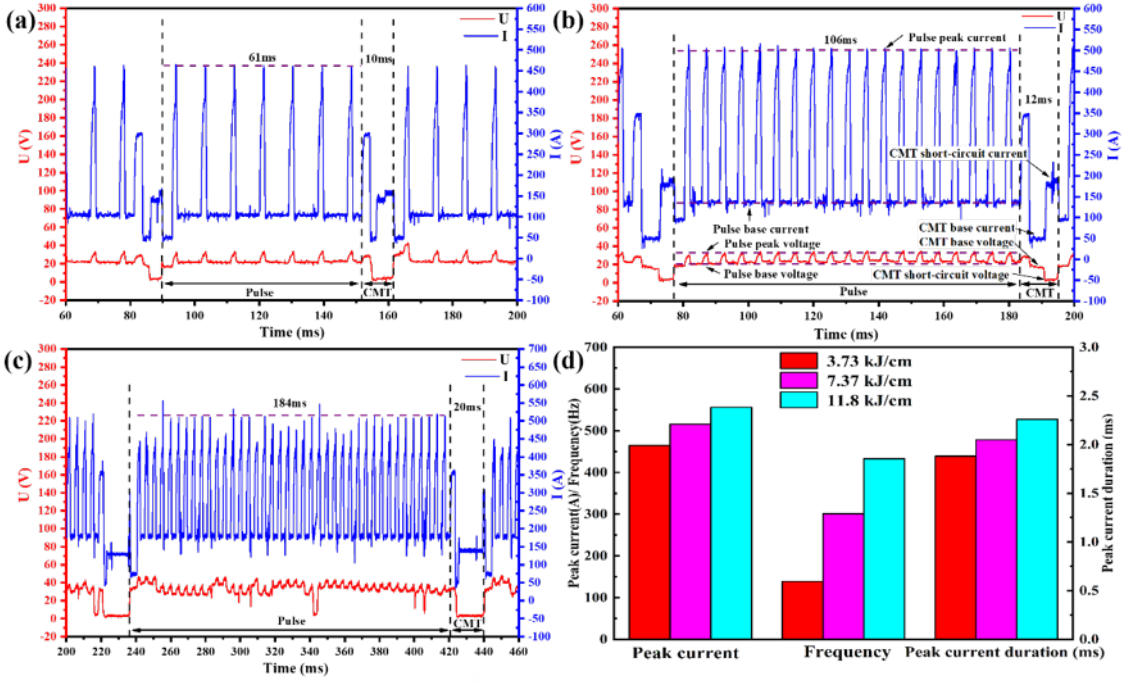


Figure 2. Current–voltage curves under different heat inputs: (a) 3.73 kJ/cm; (b) 7.37 kJ/cm; (c) 11.8 kJ /cm; (d) peak current and frequency of the pulse (left axis) and peak current duration (right axis) under different heat inputs.

expressed by **Equation 2**[35]:

$$ADR = WFS \cdot \rho \cdot \pi \cdot r^2 \quad (2)$$

where r and ρ represent the radius and density of the welding wire, respectively. As the arc deposition rate increases, the amount of metal deposited per unit time increases, the spreadability of the bead improves, the bond with the substrate becomes tighter, and the cross-sectional dimensions of the bead become significantly larger (Figure 3k).

3.2. Analysis of macrostructure and microstructure

3.2.1. Macrostructure observations

Figure 4 shows the morphology of thin-walled components under different heat inputs. At a heat input of 3.73 kJ/cm, the low heat input resulted in minimal base-metal warping, less spatter, and better forming quality. However, when the heat input increased to 7.37 kJ/cm, significant warping of the base metal appeared. At a heat input of 11.8 kJ/cm, excessive heat caused noticeable collapse and heavy spatter on the substrate, resulting in poor forming quality (Figure 4g). Under excessively high heat input, the component cross-section showed relatively poor part accuracy due to the "stair stepping" effect of WAAM, resulting in dimensional errors along the build direction. This phenomenon aligns with the trade-off between high deposition rate and high-accuracy control during WAAM manufacturing, as reported by Ding *et al.*[36] From the cross-section view, the outlines for three deposited parts are presented in Figure 4c, f, and i. Within the outline, the largest possible rectangle was drawn. The ratio of the rectangle's area to the total cross-sectional area was calculated, which can be interpreted as material efficiency.[37] The material efficiency of low-, middle-, and high-heat input samples was 82.0%, 80.7%, and 73.4%, respectively, indicating that increasing heat input may reduce forming quality.

Statistical analysis was conducted on the oxide inclusions in the microstructure of WAAM-ed components under different heat inputs using IPP software (at least 10 images). At heat inputs of 3.73 and 7.37 kJ/cm, the oxide inclusions were mainly concentrated in the 0.1~0.4 μm and 0.3~0.7 μm ranges, respectively, with area fractions of approximately 0.45% and 0.61% (**Figure 5a** & **b**). Notably, such small-volume, fine oxide inclusions can act as heterogeneous nucleation sites during solidification, thereby facilitating grain nucleation and refining the microstructure of the WAAM-ed components. When the heat input reached 11.8 kJ/cm, the oxide inclusion content increased significantly to 5.21%, 11.6 times higher

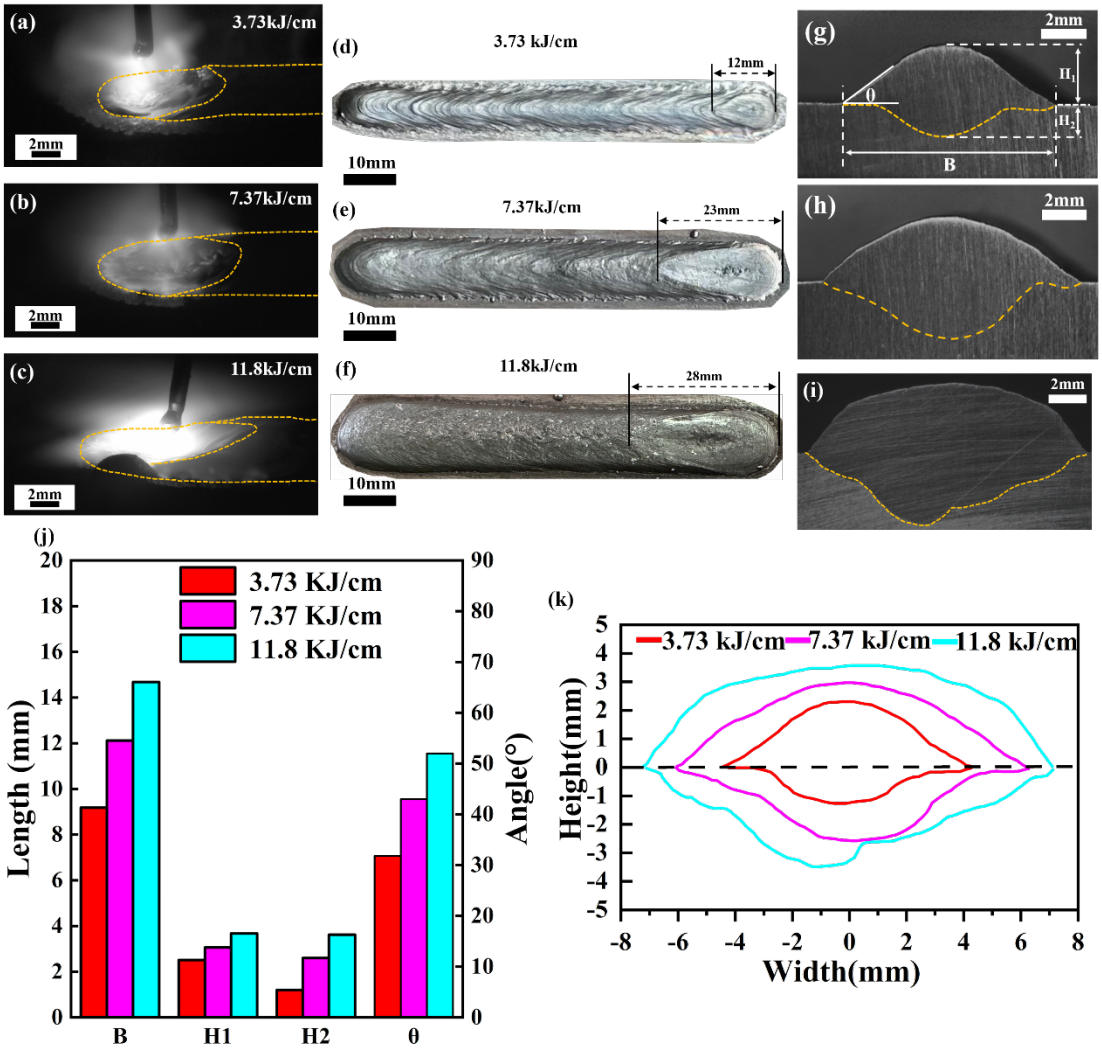


Figure 3. Effect of heat input on the molten pool, bead morphology, and cross-sectional geometry. (a–c) Molten pools under different heat inputs. Scale bar: 2 mm. (d–f) Macroscopic bead morphology under different heat inputs. Scale bar: 10 mm. (g–i) Cross-sectional morphology of the bead under different heat inputs. Scale bar: 2 mm. (j) Bead characteristics under different heat inputs. (k) Cross-sectional dimensions of the beads.

than under low heat input, and the oxide inclusions also noticeably enlarged (**Figure 5c**). Zhang *et al.*[38] reported that droplet bursting and breaking of the bell-shaped arc during deposition caused the abundant oxide inclusions in WAAM-ed materials. As illustrated in Figure 3a–c, excessive heat input results in larger molten droplets, supplying ample oxygen for the oxidation of droplets, spatters, and the molten pool, and ultimately leading to a significant rise in both the content and size range of oxide inclusions within the WAAM-ed materials. In addition, excessive oxide inclusions may reduce the mechanical properties of the deposited metal.

3.2.2. Microstructure observations

Figure 6 shows the morphology of deposition units under different heat inputs. A deposition unit consists of a deposition zone (DZ) and a remelting zone (RZ). During the WAAM process, deposition units are stacked layer by layer along the BD. When depositing the n+1 layer, the arc acts on the top of the n layer, remelting the previously solidified metal and forming a molten pool with the falling droplets. After cooling and solidification, the area above DZ n that undergoes two cycles of melting and solidification becomes RZ n+1, while the area below DZ n becomes RZ n. With increasing heat input, the deposition unit heights

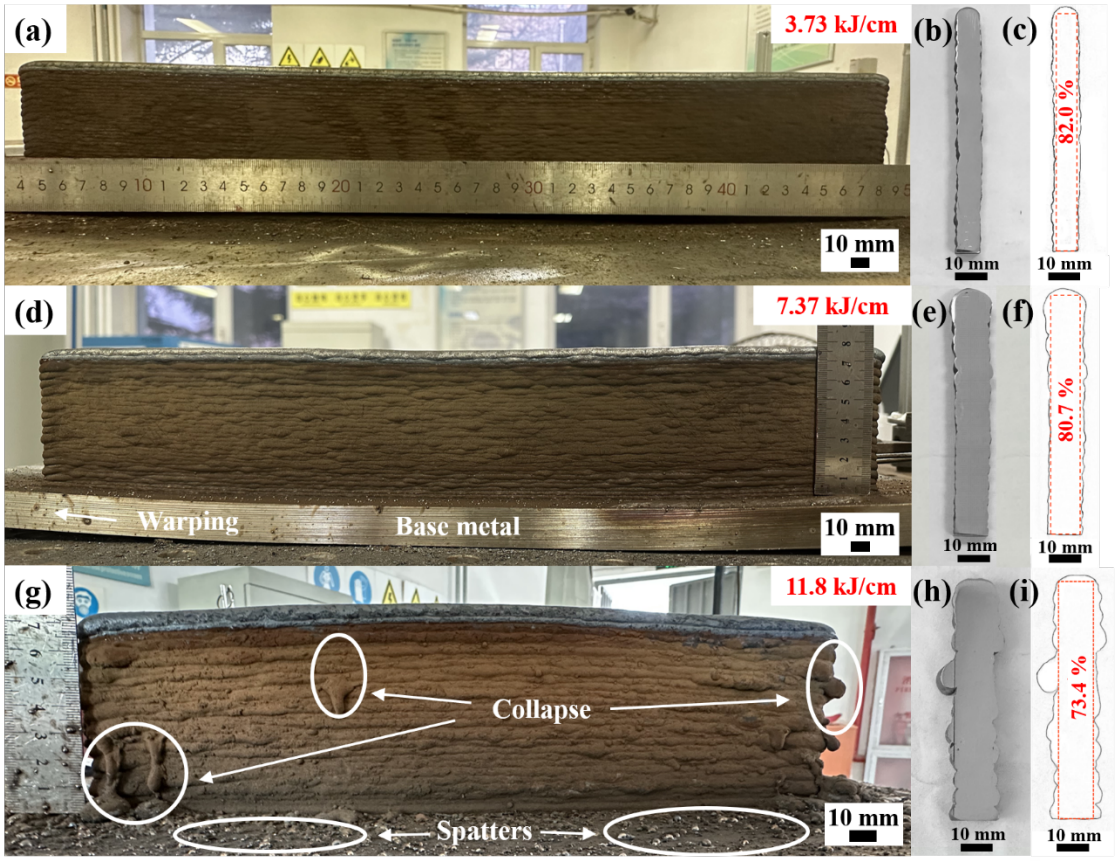


Figure 4. Wire arc additive manufactured low-alloy ultra-high-strength steel thin-walled components under different heat inputs. (a, d, g) Macroscopic morphology, (b, e, h) cross-sectional morphology, and (c, f, i) cross-section outline with the largest possible rectangular area marked with dotted red lines. Scale bar: 10 mm.

were 1.84, 2.51, and 3.05 mm, respectively, due to the higher arc deposition rate. Figure 6c, f, and i shows that the RZ is primarily composed of fine, elongated columnar grains growing perpendicular to the fusion line. This is because solidification tends to proceed along the fastest heat dissipation direction, corresponding to the steepest temperature gradient. Figure 6b, e, and h shows that the DZ is primarily composed of coarse columnar or equiaxed grains, related to the ratio of the temperature gradient (G) to the solidification rate (R)[39]. During WAAM deposition, the G/R ratio exhibits spatial variation within a single molten pool[40]. Near the fusion line, the temperature gradient G is high, and the solidification rate R is low, yielding a high G/R value that favors columnar grain growth. Moving from the fusion line toward the interior of the molten pool, G decreases while R increases, reducing the G/R ratio and promoting equiaxed grain formation. It is necessary to distinguish the solidification features of a single molten pool from microstructural characteristics under multilayer deposition. The RZ corresponds to the interlayer remelted band generated when the subsequent arc remelts the previous layer, rather than the core region of a single molten pool; hence, fine columnar grains dominate in the RZ. By contrast, the DZ corresponds to the middleupper region of every single molten pool, where coarse columnar or equiaxed grains can be observed. The statement regarding fine equiaxed grains forming at the fusion line and transitioning to columnar grains toward the moltenpool interior describes the instantaneous solidification behavior of an individual molten pool, whereas the microstructural features of RZ and DZ characterize interlayer regions subjected to repeated multilayer thermal cycling; these two descriptions address different physical objects and are not contradictory. During deposition, arc force drives hightemperature droplets to impact the molten pool at high speed, forming a circular stirring zone that breaks up growing dendrites and promotes finer dendrites or equiaxed grains. As the arc moves away, the stirring flow field weakens, and small dendrites grow perpendicular to the maximum temperature gradient. Columnar grains

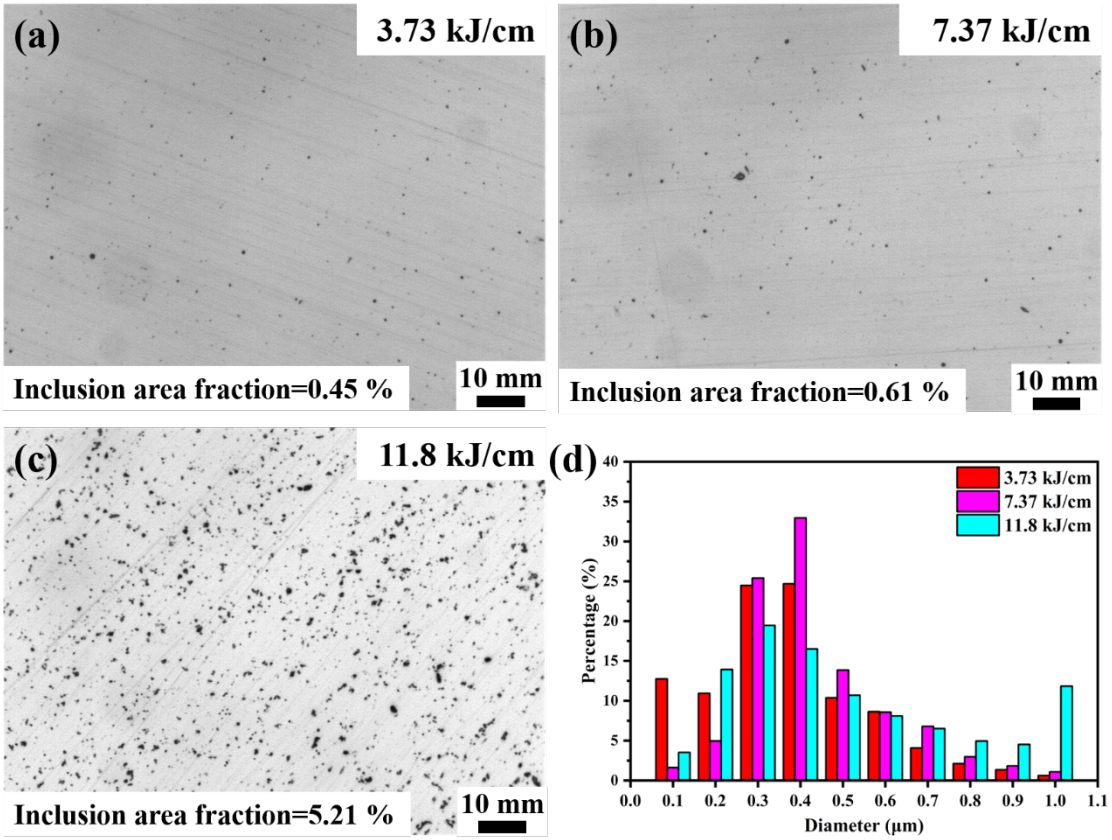


Figure 5. Oxide-inclusion characteristics under different heat inputs. (a–c) Optical microscopy images of inclusions under different heat inputs. Scale bar: 10 μm; State the magnification of the images. E.g., 10×, 20×. A scale bar indicates the actual size of structures, whereas magnification indicates how many times the image is enlarged. Please provide the appropriate information for each figure.. (d) Size distributions of oxide inclusions.

form when dendrites aligned with the temperature gradient grow faster than unoriented ones.[41] Thus, fine equiaxed grains form at the fusion line and gradually transition to columnar grains toward the next fusion line.

Figure 7 shows the OM and SEM images of thin-walled components under different heat inputs. The microstructure is mainly a mixture of lath martensite and residual austenite, with martensitic laths forming an interlocked structure. Precipitated phases of varying shapes were observed under all heat input conditions. At low heat input, the precipitates were finer and more dispersed, mainly needle-like and blocky. At 11.8 kJ/cm, precipitates were rod-like, and their quantity increased. Subsequent TEM characterization confirms these precipitates are carbides. WAAM is a layer-by-layer deposition process involving multiple thermal cycles. Subsequent layers reheat previously deposited layers above the austenitizing temperature, transforming martensite back to austenite. Upon cooling, martensite, residual austenite, and carbide particles form.[42]

To further explore the effects of different heat inputs on the grain growth and texture of the alloy, EBSD was used to characterize the samples taken from the DZ. It should be noted that the columnar and equiaxed grains observed in lowmagnification OM images (Figure 6) represent the prioraustenite solidification structures formed during WAAM deposition; after solidification, these prioraustenite grains further transformed into lathmartensite structural units (martensite packets and blocks), which are resolved in the highresolution EBSD maps in Figure 8. Figure 8a, e, and i presents the inverse pole figure maps under different heat inputs, showing that lath martensite (interlocked morphology) dominates across all conditions, consistent with SEM results. At 3.73 kJ/cm, weak *in situ* heat treatment slows grain growth, yielding an average grain size of 1.11 μm (Figure 8a). As heat input increased, grain growth accelerated, raising the average grain size to 1.32 μm and 1.48 μm (Figure 8e, i). Meanwhile, maximum texture intensity increased significantly (Figure 8b, f, j), indicating stronger grain preferred orientation and anisotropy, attributed to higher peak temperatures and severe

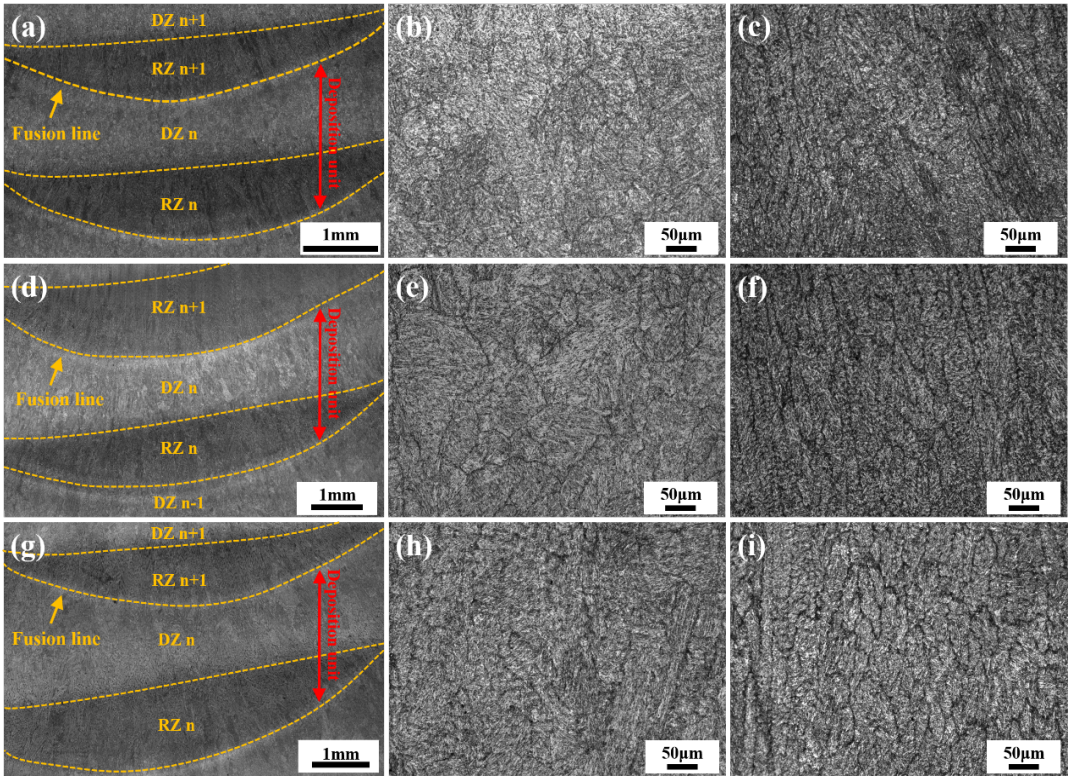


Figure 6. Optical microscope micrographs showing microstructure of low-alloy ultra-high-strength steel components at different heat inputs: (a–c) 3.73 kJ/cm, (d–f) 7.37 kJ/cm, (g–i) 11.8 kJ/cm; (b, e, h) deposition zone (DZ), (c, f, i) remelting zone (RZ). Scale bars: 1 mm, 50 μm; State the magnification of the images. E.g., 10×, 20×. A scale bar indicates the actual size of structures, whereas magnification indicates how many times the image is enlarged. Please provide the appropriate information for each figure..

thermal cycles that provide energy for grain growth and reorientation. High-angle grain boundaries (HAGBs, >15°) can be composed of austenite grains, martensitic packets, and block boundaries, while low-angle grain boundaries (LAGBs, 2~15°) are primarily formed by lath boundaries.[43] As heat input rises, the proportion of 2°~15° and >45° grain boundaries increased, while 15°~45° boundaries decreased (Figure 8c, g, k). This is because higher heat input prolongs the high-temperature dwell time, accelerating atomic diffusion, grain-boundary migration, and recrystallization. The proportion of LAGBs increases due to grain boundary migration and interactions with adjacent grains, while the proportion of HAGBs rises due to recrystallization and grain coarsening. Meanwhile, some 15°~45° grain boundaries transformed into LAGBs or were engulfed by HAGBs, reducing their relative proportion. Kernel average misorientation (KAM) was employed to represent dislocation density (Figure 8d, h, l). The KAM can represent the average misorientation between local grains; a higher KAM value corresponds to greater dislocation density.[43,44] The martensitic matrix showed high dislocation density, but the average θ_{AVG} remained constant at 0.80° across heat inputs, due to extensive carbides precipitating in martensite and at boundaries, which anchor dislocations and inhibit movement.

Figure 9a presents the XRD patterns of WAAM components under varying heat inputs. It can be observed that the microstructure is dominated by the (110) α body-centered cubic martensite phase under different heat input conditions. The face-centered cubic austenite exhibits a relatively high intensity along the (111) γ orientation, while intensities are relatively low along the (200) γ and (211) γ orientations. No diffraction peaks corresponding to precipitated phases were detected. The content of austenite was quantified using the integral intensity of XRD diffraction peaks, as shown in **Equation 3**[41]:

$$A = \sum IA / \left(\sum IM + \sum IA \right) \tag{3}$$

where A represents the fraction of retained austenite, and $\sum IA$ and $\sum IM$ represent the sum of the integrated intensities of all austenite and martensite diffraction peaks, respectively.

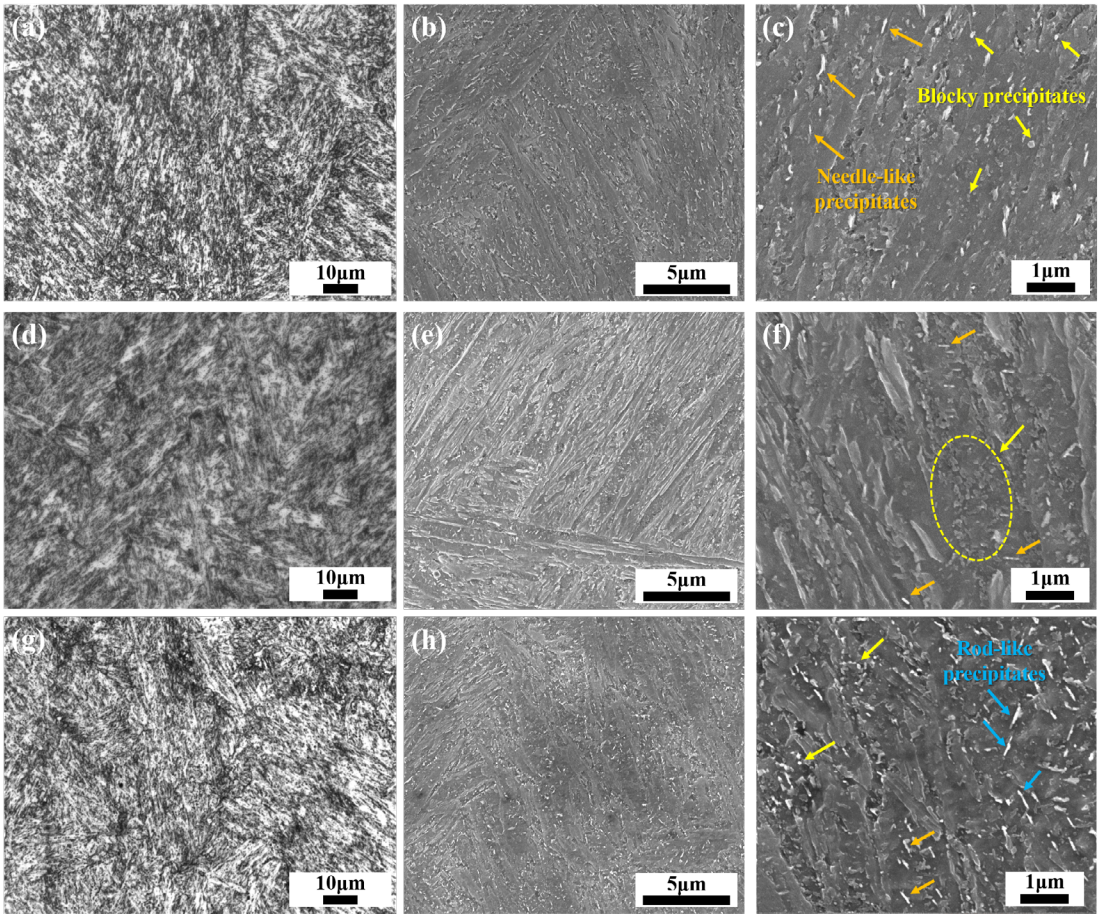


Figure 7. Optical microscopy/scanning electron microscopy images of low-alloy ultra-high-strength steel components at different heat inputs: (a–c) 3.73 kJ/cm, (d–f) 7.37 kJ/cm, (g– i) 11.8 kJ/cm. Scale bars: 1 μm, 5 μm, 10 μm; State the magnification of the images. E.g., 10×, 20×. A scale bar indicates the actual size of structures, whereas magnification indicates how many times the image is enlarged. Please provide the appropriate information for each figure..

The calculated results show that the austenite content initially increased and then decreased with increasing heat input, reaching 3.18%, 4.45%, and 2.68%, respectively (Figure 9a). This indicates that some austenite remains untransformed into martensite in the final WAAM structure. Heat input controls austenite grain growth: higher heat input prolongs dwell time above the austenitizing temperature, promoting austenite formation.[45,46] At 11.8 kJ/cm, retained austenite content decreased, likely because slower cooling allows adequate carbon diffusion, promoting its decomposition into carbides and lowering its content.

Heat input influences cooling rate, interlayer temperature, and 800°C–500°C dwell time.[26] The influence of heat input on WAAM components' microstructure mainly stems from differences in cooling rate at varying heat inputs. The cooling time of the components at different heat inputs was calculated using Vwer's empirical formula for three-dimensional heat transfer, as shown in **Equation 4**[47]:

$$t_{8/5} = \left(0.67 - 5\times10^{-4}T_0\right)\eta E\left(\frac{1}{500-T_0} - \frac{1}{800-T_0}\right)F_3 \quad (4)$$

where $t_{8/5}$ represents the cooling time of the deposited metal from 800 °C to 500 °C (s), T_0 is the initial temperature (°C, set to 120 °C), η is the relative thermal efficiency (set to 0.85), E is the energy input (J/cm), and F_3 is the three-dimensional heat transfer coefficient (set to 1). Substituting these values into **Equation 3**, the calculated $t_{8/5}$ values under different heat inputs are 2.24 s, 4.43 s, and 7.10 s, respectively. The formula for calculating the cooling rate of the deposited components is as follows (**Equation 5**):

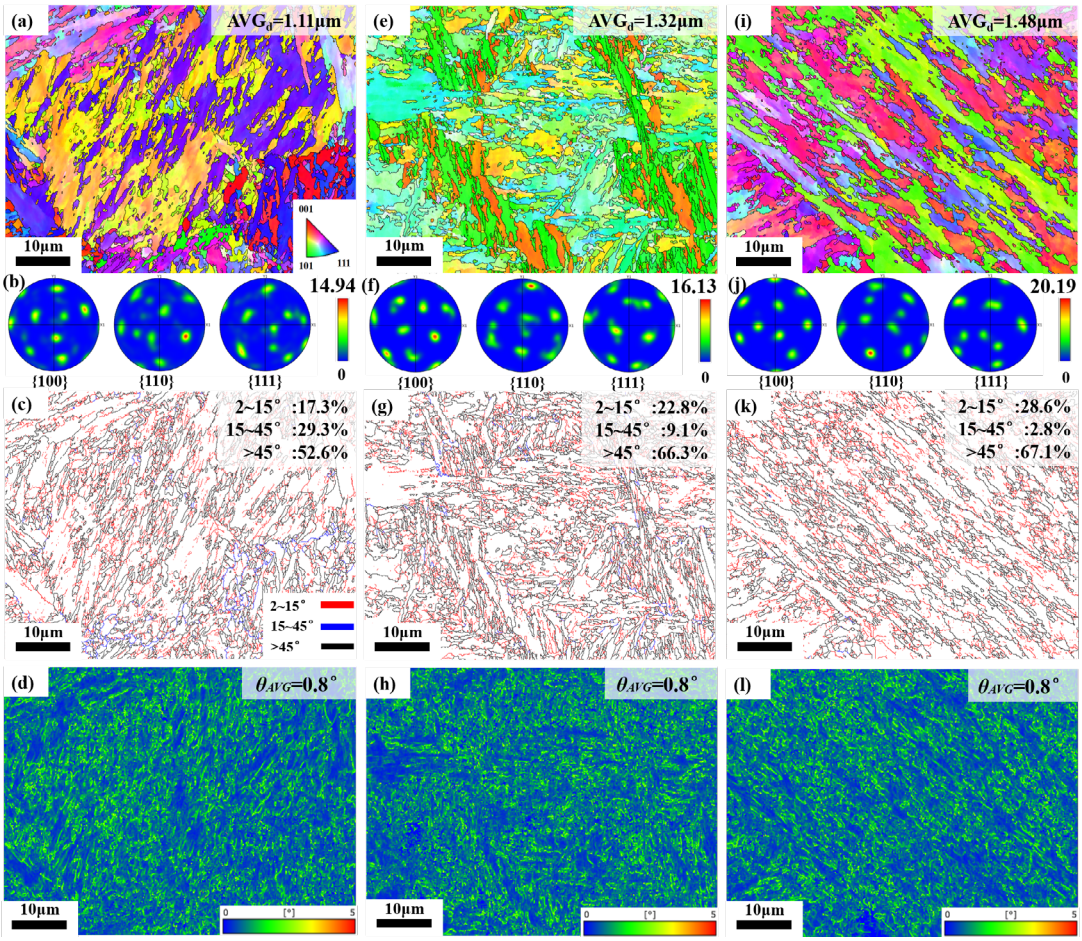


Figure 8. Electron backscatter diffraction images under different heat inputs: (a–d) 3.73 kJ/cm, (e–h) 7.37 kJ/cm, (i–l) 11.8 kJ/cm. (a, e, i) Inverse pole figures (IPFs). (b, f, j) Polar figures. (c, g, k) Grain boundaries. (d, h, l) Kernel average misorientation. Scale bar: 10 μm; State the magnification of the images. E.g., 10×, 20×. A scale bar indicates the actual size of structures, whereas magnification indicates how many times the image is enlarged. Please provide the appropriate information for each figure..

$$v_{8/5} = (800 - 500) / t_{8/5} \quad (5)$$

where $v_{8/5}$ represents the cooling rate of the deposited metal from 800 °C to 500 °C (°C/s). By substituting $t_{8/5}$ into **Equation 4**, the calculated $v_{8/5}$ values under different heat inputs are 133.93 °C/s, 67.72 °C/s, and 42.25 °C/s, respectively.

Based on the chemical composition, grain size, and austenitizing temperature of the welding wire, the continuous cooling transition curve of the LUHSS was calculated using JMatPro software, as shown in Figure 9b. The core function of this continuous cooling transition diagram is to determine whether diffusion-type phase transitions, such as bainite and pearlite, are triggered under the three actual cooling rates in this experiment. The results indicate that under all cooling rates in this study, bainite and pearlite transformation can be avoided, and the matrix mainly undergoes martensitic transformation. However, it should be pointed out that the continuous cooling transition curve only characterizes the phase transition behavior under single continuous cooling conditions and cannot explain the differences in microstructure between different samples. The differences in martensite size and the type and size of carbides in each sample mainly result from the cyclic thermal history and *in situ* tempering effect caused by WAAM multi-layer deposition, rather than a single continuous cooling process.

At a heat input of 3.73 kJ/cm, the cooling rate of the deposited metal reached 133.93 °C/s, and the undercooled austenite rapidly transformed into martensite. After increasing the heat input to 7.37 kJ/cm and 11.8 kJ/cm, the cooling rates decreased to 67.72 °C/s and 42.25 °C/s, respectively. Martensite is a non-diffusive phase

transformation, and the martensitic transformation temperature (Ms) does not change significantly with cooling rate. The diffusion behavior of alloy elements mentioned in this article is not aimed at the martensitic transformation itself, but occurs in the high-temperature range above Ms. When the cooling rate decreases, the residence time of the material in the range above the martensitic transformation temperature is prolonged, and the alloy elements are fully diffused and accompanied by carbide precipitation, causing changes in the local composition of austenite and indirectly affecting the subsequent formation of martensitic substructures, rather than changing the martensitic transformation temperature. In addition, higher interlayer temperatures can also increase the residual austenite content.[48] Although the undercooled austenite still undergoes martensitic transformation after temperature reduction, the *in situ* heat treatment effect and slower cooling rate from subsequent WAAM thermal cycling can cause incomplete phase transformation, retaining some austenite to room temperature as residual austenite.

3.3. Mechanical properties evaluation

3.3.1. Microhardness

Figure 10 presents the hardness distribution of thin-walled components along the BD under different heat inputs. The hardness values exhibited significant fluctuations, which can be attributed to the layer-by-layer deposition nature of WAAM. The average hardness values of low, middle, and high heat inputs were 483.5 HV, 475.4 HV, and 471.7 HV, respectively. Higher heat input intensifies thermal accumulation, accelerating grain coarsening and lowering average microhardness. Besides microhardness differences along the BD, periodic fluctuations exist within each deposition unit (Figure 10d). Generally, DZ exhibits higher hardness than RZ across all heat inputs, with increasing heat input significantly lowering hardness in both regions. Although the grain size within the DZ is coarser than that in the RZ, higher microhardness is observed in the DZ. This phenomenon arises from distinct microstructural evolution driven by different thermalexposure histories. The RZ undergoes intense cyclic thermal loading from successive deposited layers, leading to pronounced *in situ* tempering. Severe dislocation recovery occurs, and carbide particles coarsen substantially in the RZ, weakening both dislocationstrengthening and precipitationstrengthening contributions. Although fine grains in the RZ provide some grain-boundary strengthening, dislocation annihilation and carbide coarsening dominate the softening, resulting in lower overall microhardness. In comparison, the DZ experiences only limited thermal disturbance from subsequent layers, with mild *in situ* tempering. Accordingly, a higher dislocation density is preserved and carbides remain fine and uniformly dispersed, offering prominent contributions from dislocation strengthening and precipitation strengthening. Despite the loss of grainboundary strengthening due to coarser grains in the DZ, the combined strengthening from dislocations and fine precipitates outweighs this reduction, ultimately producing higher microhardness in the DZ. The DZ consists of relatively coarse dendritic/equiaxed grains, with limited thermal exposure (affected only by subsequent layers) and no remelting, resulting in relatively high microhardness. In contrast, RZ undergoes repeated thermal cycles from subsequent layers, forming fine, elongated columnar grains perpendicular to the fusion boundary. Notably, a high-hardness zone near the fusion line was observed

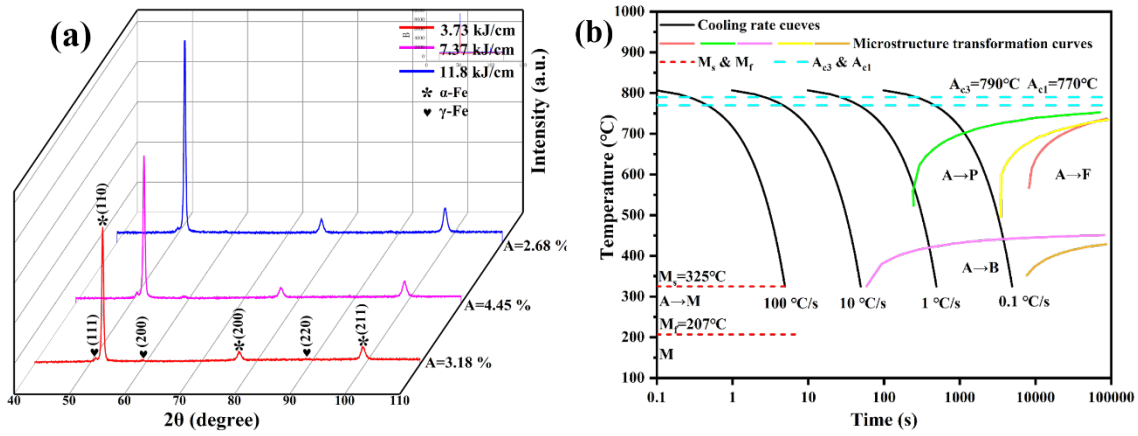


Figure 9. X-ray diffraction phase analysis and thermodynamic simulation results of thin-walled components. (a) X-ray diffraction analysis of thin-walled components under different heat inputs. (b) Continuous cooling transition (CCT) curve calculated by JmatPro.

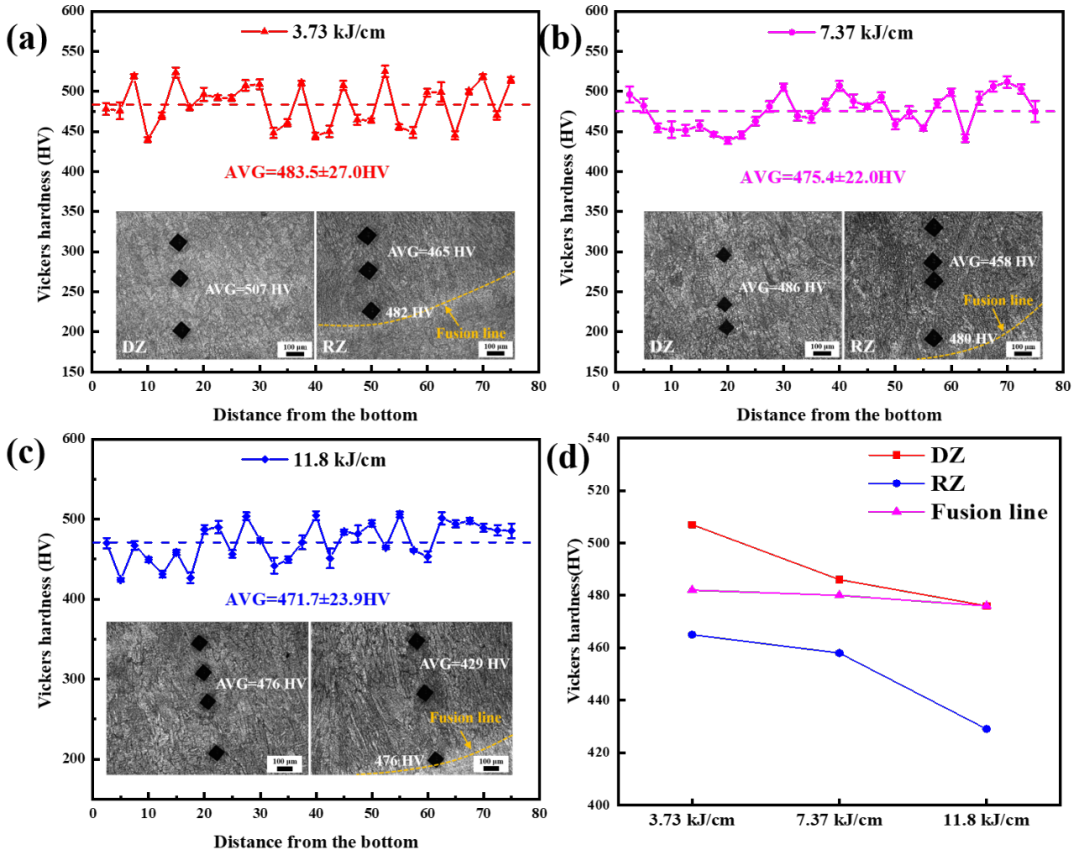


Figure 10. Microhardness results of components at different heat inputs: (a) 3.73 kJ/cm, (b) 7.37 kJ/cm, (c) 11.8 kJ/cm, (d) hardness comparison of deposition zone (DZ), remelting zone (RZ), and fusion line. Scale bar: 100 μm; State the magnification of the images. E.g., 10×, 20×. A scale bar indicates the actual size of structures, whereas magnification indicates how many times the image is enlarged. Please provide the appropriate information for each figure..

across all heat inputs. This is attributed to local remelting and recrystallization-induced grain refinement, which enhances hardness.

3.3.2. Tensile properties

Figure 11 shows the tensile properties of WAAM components under different heat inputs. As shown in Figure 11a, heat input significantly affects the mechanical properties and anisotropy of WAAM-ed LUHSS along the BD and TD. The ultimate tensile strength (UTS) increased and then decreased with increasing heat input, peaking at 1,545 MPa in the BD at 7.37 kJ/cm and dropping at 11.8 kJ/cm due to grain coarsening. The yield strength (YS) decreased continuously, peaking at 1,272 MPa at 3.73 kJ/cm. Elongation (EL) first decreased and then increased, reaching a minimum of 9.7% in the BD at 7.37 kJ/cm, while EL in the TD at 11.8 kJ/cm rebounded to 12.7%. Notably, 3.73 kJ/cm achieved a favorable balance of strength and ductility: its UTS remained at a high level (1,529 MPa in the BD, 1,506 MPa in the TD), while the EL (12.3% in the BD, 13.7% in the TD) was significantly higher than that at 7.37 kJ/cm and comparable to the TD at 11.8 kJ/cm. The in-plane anisotropy (IPA) value[49] was used to quantitatively describe the anisotropy of mechanical properties, as shown in **Equation 6**:

$$IPA = \frac{|T_{TD} - T_{BD}|}{(T_{TD} + T_{BD})/2} \times 100 \quad (6)$$

where T_{TD} is the strength in the TD, and T_{BD} is the strength in the BD.

If the IPA value is 0, the mechanical properties are isotropic. As the IPA value increases, anisotropy intensifies. As shown in Figure 11b, YS anisotropy increased with increasing heat input. Moreover, the BD exhibited higher UTS than the TD, and the TD showed better ductility under low- to medium-heat inputs. Under high heat input, the UTS anisotropy reversed, with the TD outperforming the

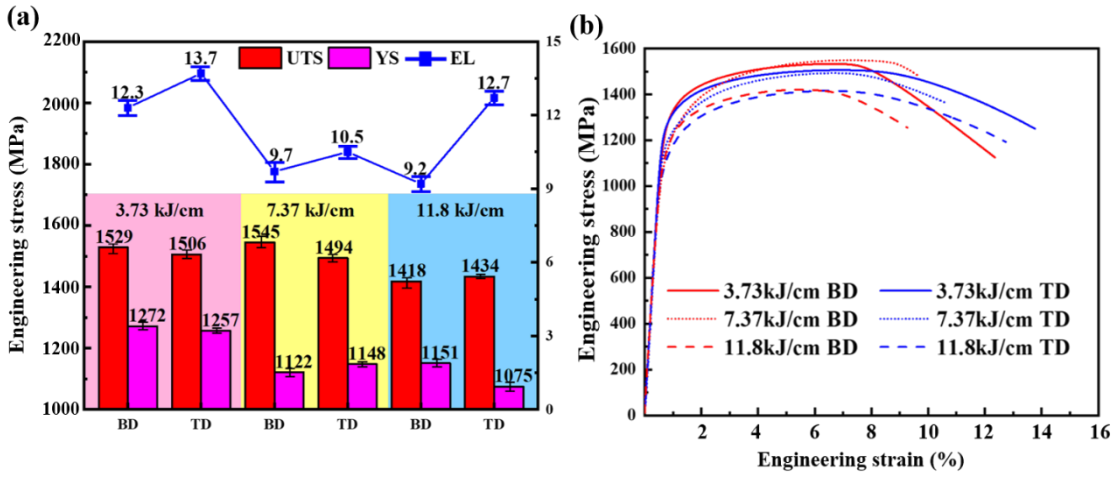


Figure 11. Comparison of tensile properties of wire arc additive manufacturing components under different heat inputs: (a) tensile properties, (b) tensile curves

BD, as elevated thermal cycles weakened the BD's preferred orientation, while the TD consistently maintained superior ductility. Overall, low heat input synergistically improved strength and ductility while reducing anisotropy.

Figure 12 shows the tensile fracture morphology of WAAM LUHSS under different heat inputs. The fracture morphology is cup-shaped and consists mainly of a fiber zone, a radiation zone, and a shear lip zone. The fiber zone corresponds to crack initiation and steady-state propagation, with a rough, uneven surface that serves as the core area for micropore nucleation, growth, and aggregation. The radiation zone corresponds to rapid, unstable crack propagation, with many secondary cracks extending along the crack path and distributed across the area. The shear lip region corresponds to the final instability stage of the fracture. At a heat input of 3.73 kJ/cm, the results show a large number of dense, uniform small dimples distributed on the fracture surface, accompanied by a small number of larger dimples. Clear tearing ridges and secondary cracks appear in the gaps between the dimples, and the fracture mode is mainly mixed ductile-brittle. Specifically, compared to the TD, the secondary cracks in the BD are deeper and more numerous, while the number and depth of toughness dimples in the TD are greater, resulting in the highest elongation in the TD. As heat input increases, the number of dimples on the fracture surface decreases, and the smaller, shallower dimples lead to lower plasticity. In addition, the appearance of cleavage planes indicates increased brittle fracture. At 11.8 kJ/cm, the cleavage plane in the BD increases, and elongation decreases by 9.2%. This may be closely related to $Cr_{23}C_6$ coarsening and the precipitation of brittle Cr_7C_3 phases. The interface bonding force between the coarsened $Cr_{23}C_6$ phase, the brittle Cr_7C_3 phase, and the martensitic matrix is weak and prone to interface debonding under tensile stress, making it the preferred site for crack initiation.

In addition, some spherical particles can be observed within the tough dimples (Figure 13), and EDS analysis indicates that the spherical particles are oxides of aluminum and titanium. Spherical particles are favorable sites for crack propagation, which can easily lead to stress concentration, inducing crack initiation and continuous propagation and reducing the material's plastic deformation capacity. The larger the spherical particles, the more likely they are to experience stress concentration, reducing plasticity.

3.4. Effects of heat input on precipitation behavior and strengthening mechanisms

3.4.1. Precipitation behavior

To clarify the precipitation evolution behavior and its correlation with mechanical properties, the microstructures of WAAM-ed LUHSS fabricated under different heat input conditions were characterized by TEM, as shown in Figure 14. The deposited microstructure mainly consists of lath martensite, retained austenite, and dispersed precipitates. As heat input increased, the martensitic lath width gradually increased from 60–180 nm to 100–250 nm and finally to 200–500 nm, indicating a weakened martensitic refinement effect under intensified thermal cycling conditions. Thin film-like structures distributed between martensitic laths were identified as retained austenite based on the selected-area electron diffraction (SAED) pattern

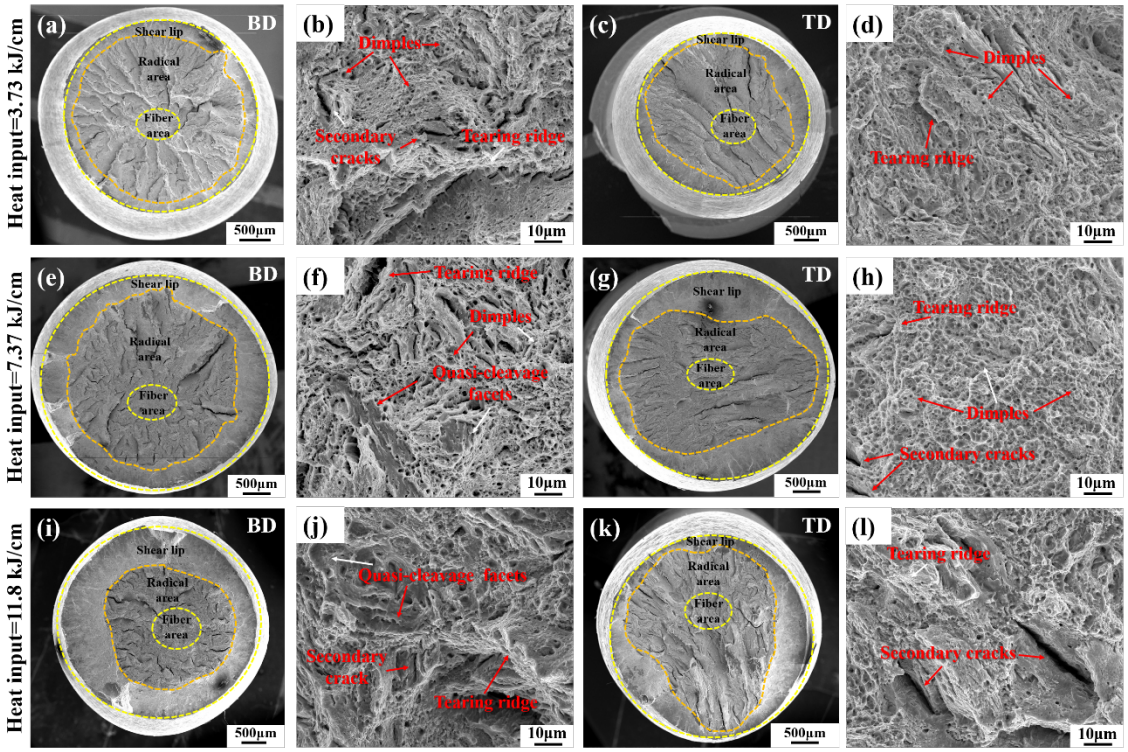
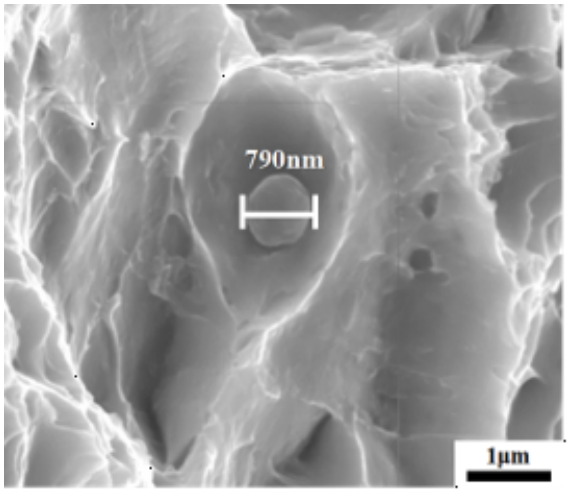


Figure 12. Fracture morphologies of tensile specimens of wire arc additive manufactured low-alloy ultra-high-strength steel at different heat inputs. (a, b, c, d) 3.73 kJ/cm; (e, f, g, h) 7.37 kJ/cm; (i-l) 11.8 kJ/cm; (a, b, e, f, i, j) building direction; (c, d, g, h, k, l) transverse direction. Scale bar: 10 μm, 500 μm; State the magnification of the images. E.g., 10×, 20×. A scale bar indicates the actual size of structures, whereas magnification indicates how many times the image is enlarged. Please provide the appropriate information for each figure..



Element	Wt%
C	6.41
O	17.7
Al	9.18
Si	0.91
Ti	2.51
Cr	2.62
Mn	1.19
Ni	0.59
Mo	0.53
W	0.6
Fe	Bal.

Figure 13. Spherical particles in dimples and their energy-dispersive spectrometer elemental analysis. Scale bar: 1 μm; State the magnification of the images. E.g., 10×, 20×. A scale bar indicates the actual size of structures, whereas magnification indicates how many times the image is enlarged. Please provide the appropriate information for each figure..

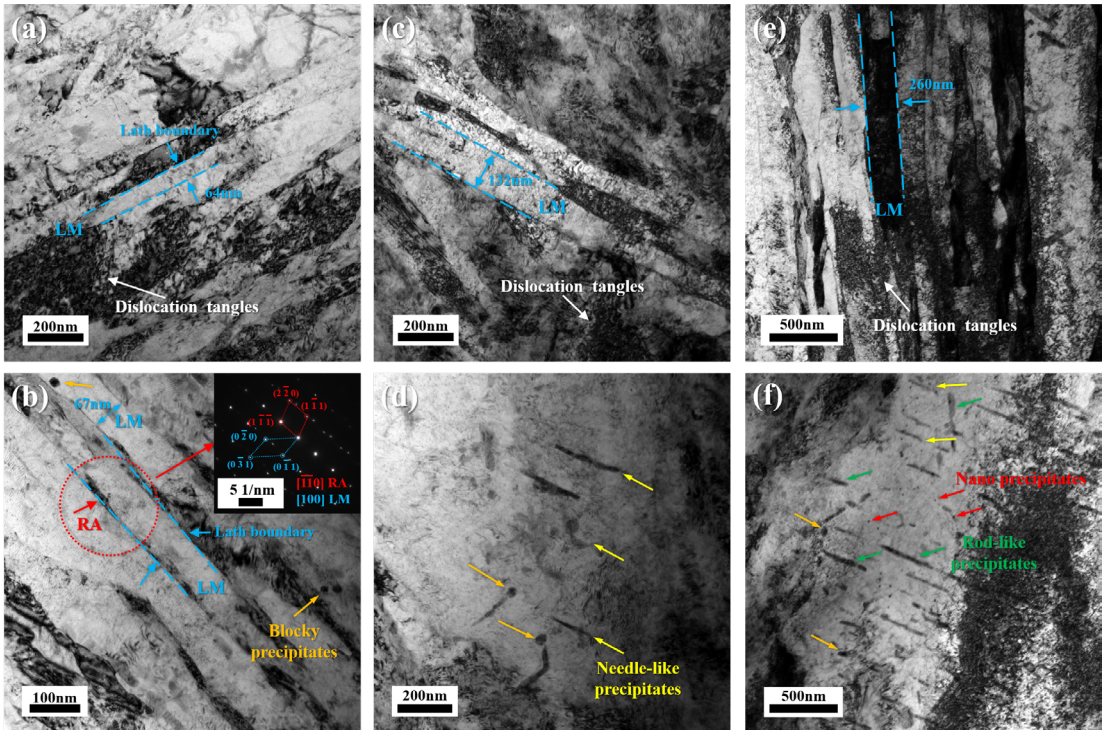


Figure 14. Transmission electron microscopy and selected-area electron diffraction characterization under different heat inputs: (a, b) 3.73 kJ/cm; (c, d) 7.37 kJ/cm; (e, f) 11.8 kJ/cm. Scale bars: 100 nm, 200 nm, 500 nm; State the magnification of the images. E.g., 10×, 20×. A scale bar indicates the actual size of structures, whereas magnification indicates how many times the image is enlarged. Please provide the appropriate information for each figure..

shown in Figure 14b. Enhanced thermal cycling and repeated reheating under high heat input intensified the *in situ* tempering effect during WAAM deposition, thereby significantly affecting precipitation and transformation behavior in the as-deposited alloy. At a heat input of 3.73 kJ/cm, the precipitates were predominantly blocky (Figure 14b). At a heat input of 7.37 kJ/cm, needle-like precipitates gradually formed (Figure 14d). Increasing the heat input to 11.8 kJ/cm significantly increased precipitate density and led to the formation of rod-like and nanoscale spherical precipitates (Figure 14f).

To further investigate the influence of heat input on the precipitation behavior of WAAM-ed LUHSS, the precipitated phases under different heat input conditions were characterized. At 3.73 kJ/cm, the precipitates were predominantly blocky (Figure 15a), with sizes ranging from 30 to 60 nm (Figure 15e). EDS analysis confirmed that the blocky precipitates consisted mainly of chromium and carbon, with minor vanadium (Figure 15c). Thermodynamic calculations using JMatPro indicated that the primary equilibrium carbides in the experimental steel were $M_{23}C_6$, M_6C, and M_7C_3, among which $M_{23}C_6$ exhibited the highest equilibrium fraction at room temperature (Figure 15d). SAED analysis further identified the precipitates as $Cr_{23}C_6$ carbides (Figure 15f), which possess a face-centered cubic crystal structure. Previous studies[50,51] reported that chromium-rich $M_{23}C_6$ carbides typically exhibit irregular, blocky morphologies ranging from 40 to 75 nm and are distributed along grain boundaries, martensitic lath boundaries, and subgrain boundaries, further supporting the identification results in this work. Notably, fine $Cr_{23}C_6$ carbides can effectively hinder dislocation motion and stabilize lath boundaries, thereby contributing to the enhanced strength of the deposited alloy[52,53].

Figure 16a shows blocky precipitates formed at a heat input of 7.37 kJ/cm, which were larger than those observed at 3.73 kJ/cm. SAED analysis identified these precipitates as $Cr_{23}C_6$ carbides. Coarsening of $Cr_{23}C_6$ precipitates could weaken the lath-boundary pinning effect, thereby reducing the strengthening contribution. In addition, needle-like precipitates with lengths ranging from 100 to 300 nm were observed (Figure 16b). EDS analysis revealed that these needle-like precipitates consisted mainly of chromium, with minor amounts of vanadium (Figure 16b_2–b_5). HRTEM and the corresponding FFT analysis further identified these precipitates as Cr_3C carbides (Figure 16c). Previous studies have reported that the M_3C

phase is hard and brittle, typically forming during low-temperature tempering (200°C–400°C), and that its size increases with increasing tempering temperature.[54] In the present work, needle-like Cr_3C precipitates with lengths of 100–300 nm were observed at a heat input of 7.37 kJ/cm (Figure 16b), and EDS analysis revealed that they mainly consisted of chromium with minor vanadium (Figure 16b$_2$–b$_5$). HRTEM and FFT analysis further confirmed their identification as Cr_3C carbides (Figure 16c). The formation of these Cr_3C precipitates is consistent with the moderate *in situ* tempering effect induced by the elevated interlayer temperature under higher heat input: repeated thermal cycling during deposition provides a tempering-like condition that promotes the diffusion of chromium and carbon atoms, which may facilitate the nucleation and growth of needlelike Cr_3C precipitates while inhibiting excessive coarsening. The needle-like morphology of Cr_3C can act as local stress concentrators, potentially hindering dislocation motion and promoting intergranular or transgranular crack propagation, consistent with the observed reduction in ductility at 7.37 kJ/cm. Together with the coarsened, blocky $Cr_{23}C_6$ carbides, these microstructural features likely contribute to the deterioration of the tensile properties and plastic deformation capacity of the WAAM-ed steel at medium heat input.

At a heat input of 11.8 kJ/cm, both coarsened chromium-rich blocky precipitates and chromium-rich rod-like precipitates were observed (Figure 17a,b). EDS analysis revealed that these rod-like precipitates primarily consist of chromium and minor vanadium (Figure 17b). The corresponding FFT result confirmed the rod-like phase as Cr_7C_3 (Figure 17d), which belongs to the hexagonal crystal system. Janovec *et al.*[55] reported that in 2.6Cr-0.7Mo-0.3V steel, the phase stability of iron–chromium-rich carbides increases with increasing tempering temperature in the sequence ε-carbides, $Fe_3C \rightarrow M_3C \rightarrow M_7C_3$. Similarly, Dong *et al.*[54] observed in microalloyed ultra-high-strength steel that the precipitation sequence follows $M_3C \rightarrow M_2C + M_3C + M_{23}C_6 \rightarrow M_2C + M_{23}C_6 + M_7C_3$ as the tempering temperature increased from 200 °C to 700 °C. In addition, another study [51] reported that under tempering conditions

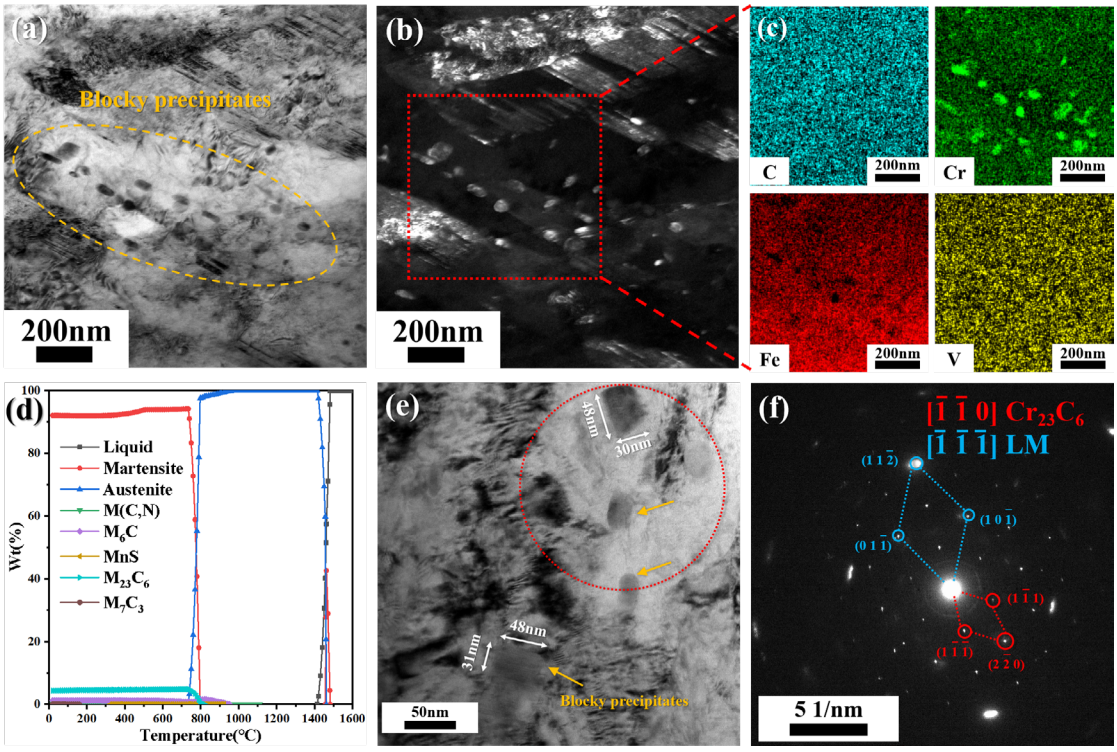


Figure 15. Transmission electron microscopy characterization at the heat input of 3.73 kJ/cm: (a) dispersed blocky precipitates under the bright field, (b) dispersed blocky precipitates under the dark field, (c) energy-dispersive spectrometer images of the blocky precipitates, (d) thermodynamic equilibrium phases calculated by JmatPro, (e) size of blocky precipitates, (f) selected-area electron diffraction pattern of the blocky precipitates. Scale bars: 50 nm, 200 nm; State the magnification of the images. E.g., 10×, 20×. A scale bar indicates the actual size of structures, whereas magnification indicates how many times the image is enlarged. Please provide the appropriate information for each figure..

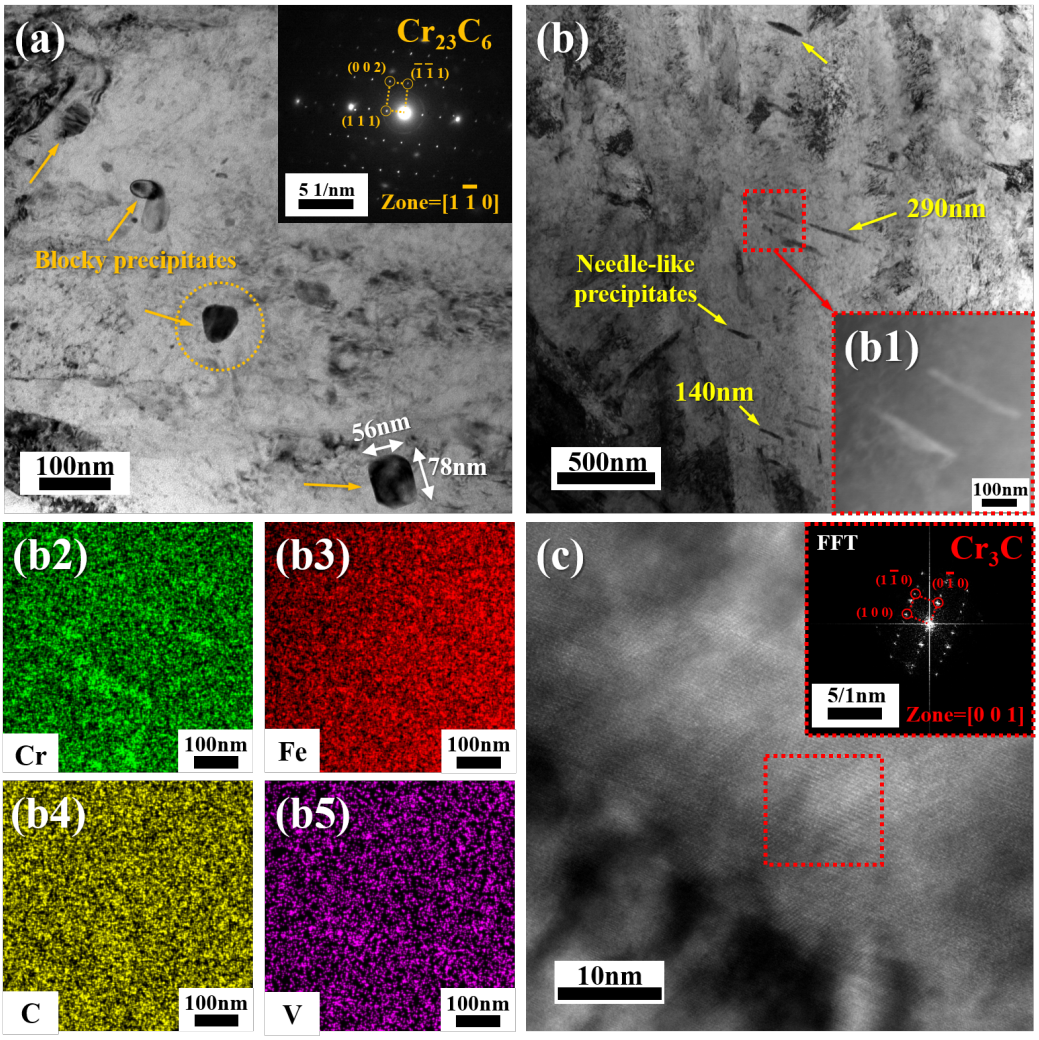


Figure 16. Transmission electron microscopy characterization (TEM) at a heat input of 7.37 kJ/cm: (a) TEM image and selected-area electron diffraction pattern of blocky precipitates, (b) needle-like precipitates, (b_1~b_5) energy-dispersive spectrometer images of the needle-like precipitates, (c) high-resolution TEM characterization and fast Fourier transform pattern of the needle-like precipitates. Scale bars: 10 nm, 100 nm, 500 nm; State the magnification of the images. E.g., 10×, 20×. A scale bar indicates the actual size of structures, whereas magnification indicates how many times the image is enlarged. Please provide the appropriate information for each figure..

at 600°C, M_3C tends to dissolve or transform into other phases, with Cr_7C_3 forming preferentially over $Cr_{23}C_6$. In the present work, increased heat input induced an intense *in situ* heat-treatment effect analogous to elevated tempering temperatures, promoting the transformation of metastable Cr_3C into rod-like Cr_7C_3 while significantly coarsening blocky $Cr_{23}C_6$. The rod-like Cr_7C_3 and coarsened $Cr_{23}C_6$ could act as local stress concentrators and weaken the lath-boundary pinning effect, collectively contributing to the reduction in UTS and YS observed at 11.8 kJ/cm. Additionally, nanoscale spherical precipitates, identified as V_2C carbides by HRTEM and FFT (Figure 17f,g), were observed in the matrix. These V_2C precipitates may enhance YS by hindering dislocation motion[56]. However, this beneficial effect is largely offset by the dominant weakening mechanisms from coarsened $Cr_{23}C_6$ and Cr_7C_3, resulting in an overall decrease in mechanical properties at high heat input.

Overall, precipitation behavior in WAAM-ed LUHSS strongly depends on heat input through the *in situ* tempering effect induced by repeated thermal cycling during layer-by-layer deposition. At the lowest heat input of 3.73 kJ/cm, the deposited alloy mainly contains fine, blocky $Cr_{23}C_6$ carbides that effectively pin martensitic lath boundaries and hinder dislocation motion, thereby

enhancing strength. At a medium heat input of 7.37 kJ/cm, coarsened $Cr_{23}C_6$ carbides coexist with needle-like Cr_3C carbides because intensified *in situ* tempering promotes local stress concentration and reduces ductility. Further increasing the heat input to 11.8 kJ/cm results in more severe thermal cycling, accompanied by the appearance of rod-like Cr_7C_3 carbides and coarsened $Cr_{23}C_6$ precipitates. Although nanoscale V_2C precipitates also formed, their strengthening contribution is insufficient to offset the detrimental effects of carbide coarsening and brittle carbide formation. These results indicate that heat input governs the type, size, and distribution of carbide precipitates, thereby regulating the strength-ductility synergy of WAAM-ed LUHSS.

3.4.2. Mechanical strengthening mechanisms

Low heat input enhances both YS and ductility in WAAM-ed LUHSS. This synergistic improvement stems from the rapid cooling rate, which disperses fine precipitates and retains a refined martensitic structure, thereby inhibiting excessive grain coarsening and balancing strength enhancement with plastic deformation capacity.

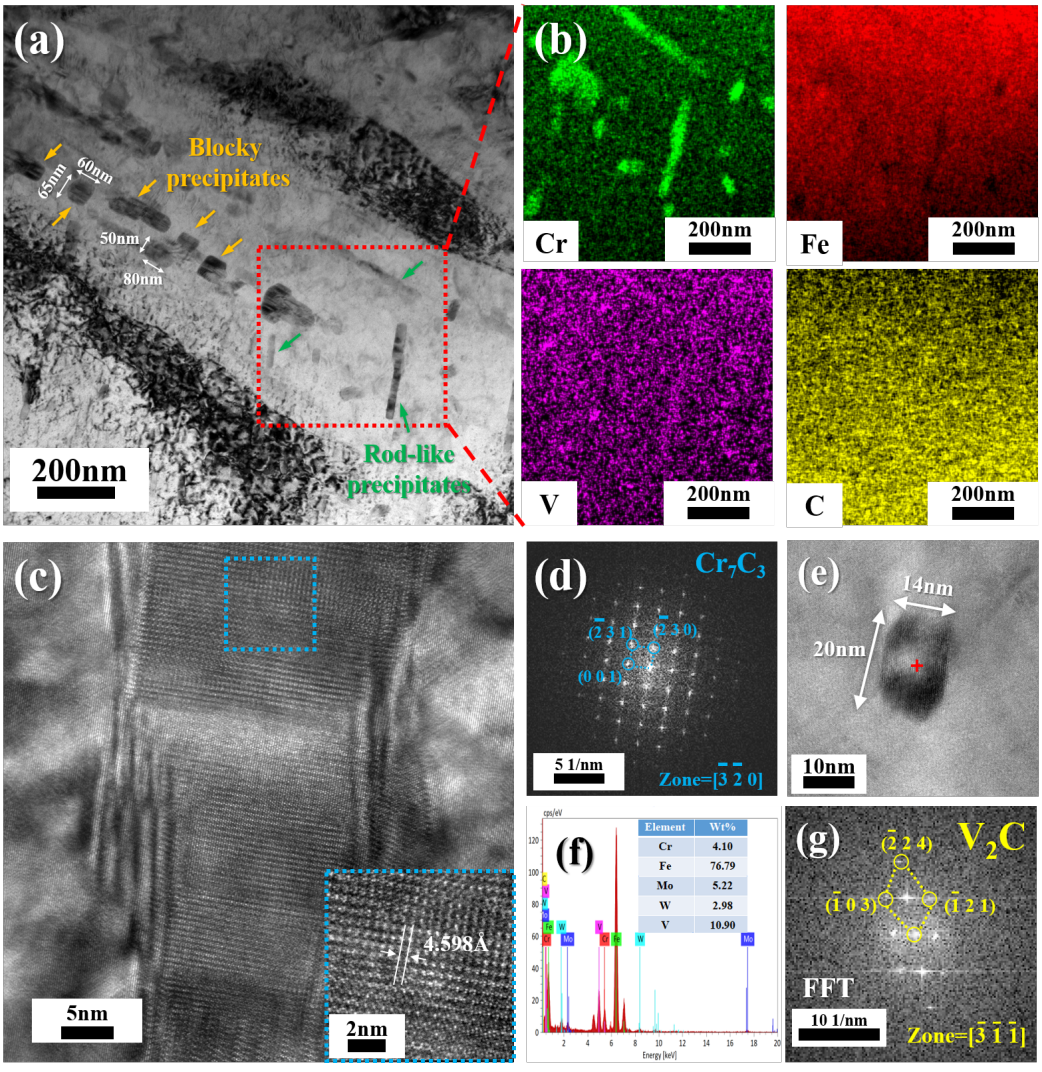


Figure 17. Transmission electron microscopy (TEM) characterization at a heat input of 11.8 kJ/cm: (a) blocky and rod-like precipitates, (b) corresponding energy-dispersive spectrometer results, (c) high-resolution TEM image of the rod-like precipitate, (d) fast Fourier transform (FFT) pattern of the rod-like precipitate, (e) nanoscale spherical precipitate, (f) energy spectrum results of the nanoscale spherical precipitate, (g) FFT pattern of the nanoscale spherical precipitate. Scale bars: 2 nm, 5 nm, 200 nm; State the magnification of the images. E.g., 10×, 20×. A scale bar indicates the actual size of structures, whereas magnification indicates how many times the image is enlarged. Please provide the appropriate information for each figure..

The strengthening mechanisms of such steels include: solid solution strengthening (σ_{ss}), grain boundary strengthening (σ_{gb}), second-phase strengthening (σ_p), and dislocation strengthening (σ_d) (**Equation 7**)[57]:

$$\sigma_y = \sigma_{ss} + \sigma_{gb} + \sigma_p + \sigma_d \quad (7)$$

The contribution of solid solution to YS (σ_y) can be calculated by the following equation (**Equation 8**)[58]:

$$\sigma_{ss} = \sum k_i c_i \quad (8)$$

where k_i is the strengthening coefficient of solute *i*, and c_i is the mass fraction of solute *i* (wt.%). According to the literature [57] and Table 3, the solid solution strengthening (σ_{ss}) under different heat inputs was calculated to be about 248 MPa.

The contribution of grain boundary strengthening to YS can be described by the Hall–Petch equation (**Equation 9**)[59]:

$$\sigma_{gb} = \sigma_0 + k_y \cdot d^{-1/2} \quad (9)$$

where σ_{gb} is the contribution of grain boundaries to YS, σ_0 is the frictional resistance, and k_y is the strengthening coefficient. According to the literatures[58,60], take σ_0 = 60 MPa, k_y =17.35 MPa mm$^{1/2}$. The grain sizes under different heat inputs are 1.11 μm, 1.32 μm, and 1.48 μm (Figure 8a, e, i), corresponding to grain boundary strengthening contributions (σ_{gb}) of 580 MPa, 537 MPa, and 510 MPa, respectively.

The influence of second-phase particles on the strength of the deposited metal can be interpreted using the Orowan–Ashby equation (**Equation 10**):

$$\sigma_p = \left(0.538Gbf^{1/2} / X\right)\ln(X/2b) \quad (10)$$

where σ_p represents the YS increment due to second-phase particles, *G* is the shear modulus, which is calculated as 82.3GPa by JmatPro, *b* is the Burgers vector (0.25nm[58]), *f* is the volume fraction of the second phase, and *X* is the diameter of the second phase. The volume fractions and diameters of the carbides under different heat inputs are statistically obtained by Image Pro Plus software as 1.67% and 52.7nm, 1.38% and 56.2 nm, and 1.92% and 76.3nm respectively. Substituting these values into the equation yields second-phase strengthening contributions (σ_p) of 126 MPa, 109 MPa, and 101 MPa.

Higher dislocation density enhances YS, particularly in martensitic microstructures with extremely high dislocation densities. The dislocation strengthening contribution (σ_d) can be calculated by the following equation (**Equation 11**)[61]:

$$\sigma_d = 0.38Gb\rho_D^{1/2} \approx 7.82\times10^{-6}\rho_D^{1/2} \quad (11)$$

where ρ_D is the dislocation density. The dislocation densities in the deposited metal at different heat inputs, calculated from XRD data, are 10.21 × 10^{14}/m^2, 9.97 × 10^{14}/m^2, and 10.08 × 10^{14}/m^2, respectively. The calculated dislocation strengthening contributions (σ_d) are 250 MPa, 247 MPa, and 248 MPa. The sum of the YS increments of the deposited metal at different heat inputs for the four strengthening methods is 1,204 MPa, 1,141 MPa, and 1,107 MPa, respectively, which is broadly consistent with the tensile test results shown in Figure 18.

Table 3. The chemical composition of wire arc additive manufactured low-alloy ultra-high-strength steel under different heat inputs in wt.%

Elements	Carbon	Silicon	Manganese	Chromium	Nickle	Molybdenum	Tungsten	Vanadium	Ferum
3.73 kJ/cm	0.25	0.84	0.69	3.28	1.11	0.77	1.00	0.19	Bal.
7.37 kJ/cm	0.25	0.85	0.68	3.22	1.08	0.76	1.00	0.19	Bal.
11.8 kJ/cm	0.25	0.86	0.72	3.23	1.09	0.78	1.00	0.18	Bal.

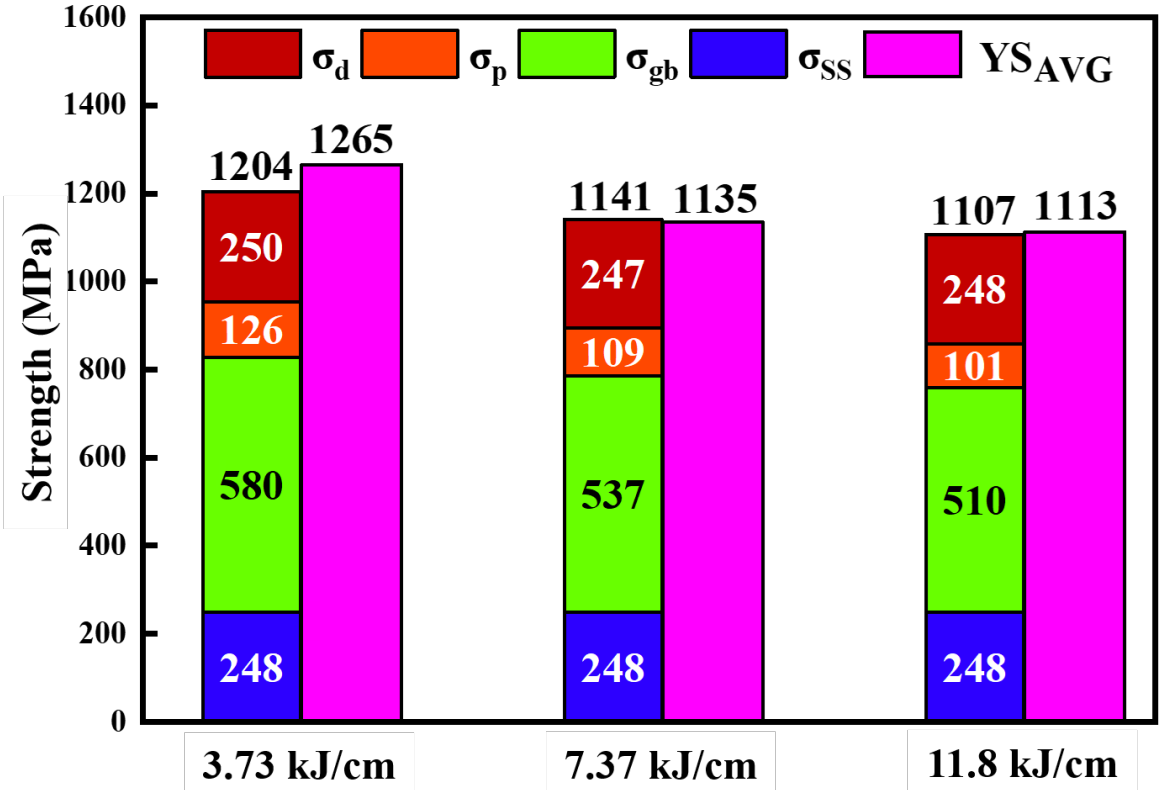


Figure 18. The strengthening increments and yield strength of deposited metals under different heat inputs

4. Conclusion

This work systematically investigated the effect of heat input on the formability, microstructure, precipitation evolution, and mechanical properties of 1,600 MPa grade LUHSS fabricated via CMT+P-based WAAM, demonstrating that tailoring heat input is an effective strategy for the synergistic control of forming quality and mechanical properties. The key conclusions are summarized as follows:

(i) Heat input strongly influences the forming quality of WAAM components. Appropriate heat input is essential for producing high-quality LUHSS parts. As heat input increases, the CMT+P cycle duration is prolonged, the arc deposition rate rises, and the weld bead dimensions expand. Low heat input ensures excellent forming quality with minimal warping and spattering, whereas excessive heat input leads to collapse, spattering, and reduced material efficiency, accompanied by a significant increase in oxide inclusions.

(ii) The microstructure is dominated by lath martensite and retained austenite across all heat inputs, but heat input modulates grain size, retained austenite content, and grain boundary characteristics. Low heat input yields a refined grain structure and moderate retained austenite content, while higher heat input accelerates grain coarsening and causes fluctuations in retained austenite content. Elevated heat input also increases the proportion of LAGBs and HAGBs, likely due to enhanced atomic diffusion and partial recrystallization.

(iii) Heat input control significantly affects the strength and anisotropy of WAAM-ed LUHSS. Optimal strength–ductility synergy (UTS: 1529 MPa, YS: 1272 MPa, elongation: 12.3%) and near-isotropic mechanical properties were achieved at 3.73 kJ/cm. The primary strengthening mechanisms include grain boundary strengthening, dislocation strengthening, and second-phase (precipitation) strengthening. Higher heat input reduces microhardness and YS.

(iv) Heat input influences the type, size, and distribution of precipitates, most plausibly via varying degrees of *in situ* tempering originating from repeated layerbylayer thermal cycling. At 3.73 kJ/cm, blocky $Cr_{23}C_6$ precipitates dominate. At 7.37 kJ/cm, needlelike Cr_3C precipitates are observed. At 11.8 kJ/cm, rodlike Cr_7C_3 and nanoscale V_2C precipitates can be detected. These carbiderelated microstructural features are associated

with tensilefracture behavior, where coarse, brittle carbides may act as stressconcentration sites and reduce ductility.

Acknowledgments

None.

Funding

Authors acknowledge the support from National Natural Science Foundation of China (52475324, 52505341), Fundamental Research Founds for the National Key Research and Development Program of China (2023YFB3408003). Central Universities (2024IAIS-QN012), Chongqing Technology Innovation and Application Development Special Major Project (CSTB2024TIAD-STX0016), New Chongqing Youth Innovative Talents Project (CSTB2024NSCQ-QCXMX0082), Innovation Support Program for Overseas Returnees in Chongqing (cx2023061), Natural Science Foundation of Chongqing (CSTB2024NSCQ-MSX1072), Natural Science Foundation of Hubei Province (2025AFD095), National Key R&D Program of China (No. 2024YFB4609700).

Conflict of interest

The authors declare no known competing financial interests or personal relationships that could have influenced the work reported in this paper.

Author contributions

Conceptualization: Kun Li, Shuangjun Zhang, Ziche Li, Shixin Xu, Xuru Hou, Peng Li,
Xiangrui Wan, Liang Zhu
Data curation: Shuangjun Zhang, Ziche Li
Funding acquisition: Kun Li, Lin Zhao, Liang Zhu
Investigation: Shuangjun Zhang, Ziche Li, Shixin Xu, Xuru Hou, Chen Ji
Project administration: Yang Cao, Lin Zhao
Methodology: Kun Li, Shuangjun Zhang, Ziche Li, Shixin Xu, Xuru Hou, Peng Li,
Xiangrui Wan, Liang Zhu, Chen Ji, Yang Cao, Lin Zhao
Resources: Kun Li, Lin Zhao, Chengyong Ma, Zhiling Tian
Supervision: Kun Li, Liang Zhu, Chengyong Ma, Zhiling Tian
Writing–original draft: Kun Li, Shuangjun Zhang
Writing–review & editing: Kun Li, Xuru Hou, Peng Li, Xiangrui Wan, Liang Zhu, Chen Ji, Yang Cao, Lin Zhao, Chengyong Ma, Zhiling Tian

Ethics approval and consent to participate

Not applicable.

Consent for publication

Not applicable.

Availability of data

Data are available from the corresponding author upon reasonable request.

References

1. Li K, Yang T, Gong N, *et al.* Additive manufacturing of ultra-high strength steels: A review. *J Alloys Compd.* 2023;965:171390.

   doi: 10.1016/j.jallcom.2023.171390

2. Tümer M, Schneider-Bröskamp C, Enzinger N. Fusion welding of ultra-high strength structural steels – A review. *J Manuf Processes.* 2022;82:203-229.

   doi: 10.1016/j.jmapro.2022.07.049

3. Duan Y, Zhu W, Liu W, Ma Y, Cai Q, Cai Y. A novel strategy for preparing high-performance powder metallurgical low alloy ultrahigh strength steel. *Mater Sci Eng A.* 2023;864:144585.

   doi: 10.1016/j.msea.2023.144585

4. Choudhary SK, Ganguly S, Sengupta A, Sharma V. Solidification morphology and segregation in continuously cast steel slab. *J Mater Process Technol.* 2017;243:312-321.

   doi: 10.1016/j.jmatprotec.2016.12.030

5. Li K, Liao R, Zheng Q, *et al.* Design exploration of staggered hybrid minimal surface magnesium alloy bone scaffolds. *Int J Mech Sci.* 2024;281:109566.

   doi: 10.1016/j.ijmecsci.2024.109566

6. Zhan J, Li Y, Guo Z, *et al.* A 4D-printed NiTi alloy with encoded microstructures evades the cooling capacity–energy efficiency trade-off in elastocaloric refrigeration. *Mater Sci Eng R Rep.* 2026;169:101191.

   doi: 10.1016/j.mser.2026.101191

7. Treutler K, Wesling V. The Current State of Research of Wire Arc Additive Manufacturing (WAAM): A Review. *Appl Sci.* 2021;11(18):8619.

   doi: 10.3390/app11188619

8. Jafari D, Vaneker THJ, Gibson I. Wire and arc additive manufacturing: Opportunities and challenges to control the quality and accuracy of manufactured parts. *Mater Des.* 2021;202:109471.

   doi: 10.1016/j.matdes.2021.109471

9. Jing C, Chen Z, Liu B, *et al.* Improving mechanical strength and isotropy for wire-arc additive manufactured 304L stainless steels via controlling arc heat input. *Mater Sci Eng A.* 2022;845:143223.

   doi: 10.1016/j.msea.2022.143223

10. Le VT, Bui MC, Nguyen TD, Nguyen VA, Nguyen VC. On the connection of the heat input to the forming quality in wire-and-arc additive manufacturing of stainless steels. *Vacuum.* 2023;209:111807.

doi: 10.1016/j.vacuum.2023.111807

11. Panagiotopoulos V, Hadjipantelis N, Gantes CJ. Influence of process parameters on weld quality and nominal geometry of wire arc additively manufactured steel elements. *Structures.* 2025;80:110044.

doi: 10.1016/j.istruc.2025.110044

12. Gupta DK, Mulik RS. Selection of Process Parameters and its Effect on Bead Geometry, Mechanical Properties, and Microstructure of Inconel 825 Fabricated Using Wire Arc Additive Manufacturing. *Met Mater Int.* 2025;31(12):3744-3760.

doi: 10.1007/s12540-025-01967-y

13. Zhang J, Fan J, Xu J, Yang D, Peng Y, Wang K. The effect of heat input on the microstructure and mechanical properties of 18Ni 300 maraging steel fabricated by arc directed energy deposition. *Mater Sci Eng A.* 2023;884:145545.

doi: 10.1016/j.msea.2023.145545

14. Deng F, Yang G, Wu B, Qin L, Zheng J, Zhou S. Microstructure and Mechanical Properties of Hybrid-Manufactured Maraging Steel Component Using 4% Nitrogen Shielding Gas Fabricated by Wrought-Wire Arc Additive Manufacturing. *Coatings.* 2022;12(3):356.

doi: 10.3390/coatings12030356

15. Kachomba T, Mutua J, Obiko J, Ngoret J. Multi-response optimisation of wire-arc additive manufacturing process parameters for AISI 4130 steel during remanufacturing process. *Mater Res Express.* 2024;11(5):056503.

doi: 10.1088/2053-1591/ad425a

16. Zhao J, Quan G-z, Zhang Y-q, *et al.* Influence of deposition path strategy on residual stress and deformation in weaving wire-arc additive manufacturing of disc parts. *J Mater Res Technol.* 2024;30:2242-2256.

doi: 10.1016/j.jmrt.2024.03.226

17. Knezović N, Garašić I, Jurić I. Influence of the Interlayer Temperature on Structure and Properties of Wire and Arc Additive Manufactured Duplex Stainless Steel Product. *Materials.* 2020;13(24):5795.

doi: 10.3390/ma13245795

18. Turgut B, Gürol U, Onler R. Effect of interlayer dwell time on output quality in wire arc additive manufacturing of low carbon low alloy steel components. *Int J Adv Manuf Tech.* 2023;126(11-12):5277-5288.

doi: 10.1007/s00170-023-11481-3

19. Sun L, Jiang F, Huang R, Yuan D, Guo C, Wang J. Anisotropic mechanical properties and deformation behavior of low-carbon high-strength steel component fabricated by wire and arc additive manufacturing. *Mater Sci Eng A.* 2020;787:139514.

doi: 10.1016/j.msea.2020.139514

20. Rafieazad M, Nemani AV, Ghaffari M, Nasiri A. On Microstructure and Mechanical Properties of a Low-Carbon Low-Alloy Steel Block Fabricated by Wire Arc Additive Manufacturing. *J Mater Eng Perform.* 2021;30(7):4937-4945.

doi: 10.1007/s11665-021-05568-9

21. Farias FWC, da Cruz Payão Filho J, Moraes e Oliveira VHP. Prediction of the interpass temperature of a wire arc additive manufactured wall: FEM simulations and artificial neural network. *Addit Manuf.* 2021;48:102387.

doi: 10.1016/j.addma.2021.102387

22. Zeng J, Nie W, Li X. The Influence of Heat Input on the Surface Quality of Wire and Arc Additive Manufacturing. *Appl Sci.* 2021;11(21):10201.

doi: 10.3390/app112110201

23. Rosli NA, Alkahari MR, Abdollah MFb, Maidin S, Ramli FR, Herawan SG. Review on effect of heat input for wire arc additive manufacturing process. *J Mater Res Technol.* 2021;11:2127-2145.

doi: 10.1016/j.jmrt.2021.02.002

24. Yildiz AS, Davut K, Koc B, Yilmaz O. Wire arc additive manufacturing of high-strength low alloy steels: study of process parameters and their influence on the bead geometry and mechanical characteristics. *Int J Adv Manuf Tech.* 2020;108(11-12):3391-3404.

doi: 10.1007/s00170-020-05482-9

25. Fang Q, Zhao L, Chen C, Zhu Y, Peng Y, Yin F. Effect of heat input on microstructural and mechanical properties of high strength low alloy steel block parts fabricated by wire arc additive manufacturing. *Mater Today Commun.* 2023;34:105146.

doi: 10.1016/j.mtcomm.2022.105146

26. Rodrigues TA, Duarte V, Avila JA, Santos TG, Miranda RM, Oliveira JP. Wire and arc additive manufacturing of HSLA steel: Effect of thermal cycles on microstructure and mechanical properties. *Addit Manuf.* 2019;27:440-450.

doi: 10.1016/j.addma.2019.03.029

27. Duarte VR, Rodrigues TA, Schell N, Santos TG, Oliveira JP, Miranda RM. Wire and Arc Additive Manufacturing of High-Strength Low-Alloy Steel: Microstructure and Mechanical Properties. *Adv Eng Mater.* 2021;23(11):2001036.

doi: 10.1002/adem.202001036

28. Rashid MS. High-Strength, Low-Alloy Steels. *Science.* 1980;208(4446):862-869.

doi: 10.1126/science.208.4446.862

29. Li J, Zhan D, Jiang Z, Zhang H, Yang Y, Zhang Y. Progress on improving strength-toughness of ultra-high strength martensitic steels for aerospace applications: a review. *J Mater Res Technol.* 2023;23:172-190.

doi: 10.1016/j.jmrt.2022.12.177

30. Xu Y, Mishra B, Narra SP. Experimental investigation of in-situ microstructural transformations in wire arc additively manufactured maraging 250-grade steel. *Mater Charact.* 2022;190:112065.

doi: 10.1016/j.matchar.2022.112065

31. Hearn W, Lindgren K, Persson J, Hryha E. In situ tempering of martensite during laser powder bed fusion of Fe-0.45C steel. *Materialia.* 2022;23:101459.

doi: 10.1016/j.mtla.2022.101459

32. Gou Q, Zhang Z, Xu L, Wu D, Zhang T, Liu H. Heat and mass transfer behavior in CMT plus pulse arc manufacturing. *Int J Mech Sci.* 2024;281:109638.

doi: 10.1016/j.ijmecsci.2024.109638

33. Pang J, Hu S, Shen J, Wang P, Liang Y. Arc characteristics and metal transfer behavior of CMT+P welding process. *J Mater Process Technol.* 2016;238:212-217.

doi: 10.1016/j.jmatprotec.2016.07.033

34. Luo Y, Li J, Xu J, Zhu L, Han J, Zhang C. Influence of pulsed arc on the metal droplet deposited by projected transfer mode in wire-arc additive manufacturing. *J Mater Process Technol.* 2018;259:353-360.

doi: 10.1016/j.jmatprotec.2018.04.047

35. Han Q, Gao J, Han C, Zhang G, Li Y. Experimental investigation on improving the deposition rate of gas metal arc-based additive manufacturing by auxiliary wire feeding method. *Weld World.* 2021;65(1):35-45.

doi: 10.1007/s40194-020-00994-0

36. Ding D, Pan Z, Cuiuri D, Li H. Wire-feed additive manufacturing of metal components: technologies, developments and future interests. *Int J Adv Manuf Tech.* 2015;81(1-4):465-481.

doi: 10.1007/s00170-015-7077-3

37. Ahsan MRU, Seo G-J, Fan X, *et al.* Effects of process parameters on bead shape, microstructure, and mechanical properties in wire + arc additive manufacturing of Al0.1CoCrFeNi high-entropy alloy. *J Manuf Processes.* 2021;68:1314-1327.

doi: 10.1016/j.jmapro.2021.06.047

38. Zhang X, Zhao Q, Liu C, *et al.* On the formation of oxide inclusions in the high nitrogen chromium-manganese steel produced by the Wire and Arc Additive Manufacturing. *J Mater Res Technol.* 2024;33:3852-3863.

doi: 10.1016/j.jmrt.2024.10.103

39. Zhan J, Li K, Ma R, *et al.* Achieving fine tailoring of elastocaloric properties of laser powder bed-fused NiTi alloy via laser beam manipulation. *Int J Mach Tools Manuf.* 2024;202:104210.

doi: 10.1016/j.ijmachtools.2024.104210

40. Guo L, Lina Z, Joel A, and Ojo O. Solidification structures and phases in wire arc additive manufactured C250 maraging steel. *Mater Sci Technol.* 2023;39(5):582-590.

doi: 10.1080/02670836.2022.2128577

41. Kan C, Zhao L, Cao Y, Ma C, Peng Y, Tian Z. Microstructure evolution and strengthening behavior of maraging steel fabricated by wire arc additive manufacturing at different heat treatment processes. *Mater Sci Eng A.* 2024;909:146804.

doi: 10.1016/j.msea.2024.146804

42. Ali Y, Henckell P, Hildebrand J, Reimann J, Bergmann JP, Barnikol-Oettler S. Wire arc additive manufacturing of hot work tool steel with CMT process. *J Mater Process Technol.* 2019;269:109-116.

doi: 10.1016/j.jmatprotec.2019.01.034

43. Lyu Z, Sato YS, Tokita S, Zhao Y, Jia J, Wu A. Microstructural evolution in a thin wall of 2Cr13 martensitic stainless steel during wire arc additive manufacturing. *Mater Charact.* 2021;182:111520.

doi: 10.1016/j.matchar.2021.111520

44. Li K, Zhan J, Yang T, *et al.* Homogenization timing effect on microstructure and precipitation strengthening of 17–4PH stainless steel fabricated by laser powder bed fusion. *Addit Manuf.* 2022;52:102672.

doi: 10.1016/j.addma.2022.102672

45. Tasalloti H, Kah P, Martikainen J. Effect of heat input on dissimilar welds of ultra high strength steel and duplex stainless steel: Microstructural and compositional analysis. *Mater Charact.* 2017;123:29-41.

doi: 10.1016/j.matchar.2016.11.014

46. Zheng Y, Liu F, Gao J, *et al.* Effect of different heat input on the microstructure and mechanical properties of laser cladding repaired 300M steel. *J Mater Res Technol.* 2023;22:556-568.

doi: 10.1016/j.jmrt.2022.11.153

47. Rust B, Schmidt J, Stroetmann R. Influence of the cooling time t8/5 on weld metals. *Weld World.* 2025;69(10):2961-2974.

doi: 10.1007/s40194-025-01942-6

48. Ge J, Lin J, Fu H, Lei Y, Xiao R. Tailoring microstructural features of wire arc additive manufacturing 2Cr13 part via varying inter-layer dwelling time. *Mater Lett.* 2018;232:11-13.

doi: 10.1016/j.matlet.2018.08.037

49. Deng M, Sui S, Yao B, Ma L, Lin X, Chen J. Microstructure

and room-temperature tensile property of Ti-5.7Al-4.0Sn-3.5Zr-0.4Mo-0.4Si-0.4Nb-1.0Ta-0.05C with near equiaxed β grain fabricated by laser directed energy deposition technique. *J Mater Sci Technol.* 2022;101:308-320.

doi: 10.1016/j.jmst.2021.03.012

50. Kishida K, Ito M, Inui H, Heilmaier M, Eggeler G. On the inherent strength of Cr23C6 with the complex face-centered cubic D84 structure. *Acta Mater.* 2024;263:119518.

doi: 10.1016/j.actamat.2023.119518

51. Shen Y, Wo J. M3C2 (Cr3C2 Type) carbides formed in steel. *Mater Today Commun.* 2023;35:106280.

doi: 10.1016/j.mtcomm.2023.106280

52. Zheng L, Hu X, Kang X, Li D. Precipitation of M23C6 and its effect on tensile properties of 0.3C–20Cr–11Mn–1Mo–0.35N steel. *Mater Des.* 2015;78:42-50.

doi: 10.1016/j.matdes.2015.04.016

53. Qiu J, He X, Liu Z, Tang Z, Wang X, He J. Effect of W and Mo contents on the microstructural evolution and properties in the 9% Cr martensitic rotor steel during long-term aging at 630 °C. *J Mater Res Technol.* 2024;32:152-164.

doi: 10.1016/j.jmrt.2024.07.069

54. Dong J, Zhou X, Liu Y, Li C, Liu C, Guo Q. Carbide precipitation in Nb-V-Ti microalloyed ultra-high strength steel during tempering. *Mater Sci Eng A.* 2017;683:215-226.

doi: 10.1016/j.msea.2016.12.019

55. Janovec J, Vyrostkova A, Svoboda M. Influence of tempering temperature on stability of carbide phases in 2.6cr-0.7mo-0.3v steel with various carbon content. *Article. Metall Mater Trans A.* 1994;25(2):267-275.

doi: 10.1007/BF02647972

56. Zhou Z, Shan Q, Jiang Y, Li Z, Zhang Z. Effect of nanoscale V2C precipitates on the three-body abrasive wear behavior of high-Mn austenitic steel. *Wear.* 2019;436-437:203009.

doi: 10.1016/j.wear.2019.203009

57. Galindo-Nava EI, Rivera-Díaz-del-Castillo PEJ. A model for the microstructure behaviour and strength evolution in lath martensite. *Acta Mater.* 2015;98:81-93.

doi: 10.1016/j.actamat.2015.07.018

58. Yao Z, Huang Z, Lyu S, Tang F, Zhao B, Ma X. Characterization and strengthening mechanism of high-strength medium carbon spring steels. *J Mater Res Technol.* 2023;27:1395-1405.

doi: 10.1016/j.jmrt.2023.09.314

59. Petch NJ. The cleavage strength of polycrystals. *J Iron Steel Inst.* 1953;174:25-28.

60. Guo W, An T, Zheng S, Zuo Y, Cao Z, Ma C. Influence mechanism of PWHT on strength and toughness of deposited metal with 1500 MPa grade ultra-high strength steel welding wire. *Mater Sci Eng A.* 2025;925:147846.

doi: 10.1016/j.msea.2025.147846

61. Kang J, Zhao L, An T, Cao Z, Zuo Y, Ma C. Effect of carbon content on strength and toughness of deposited metal for 1000 MPa-grade high-strength welding wire. *Mater Today Commun.* 2024;39:108930.

doi: 10.1016/j.mtcomm.2024.108930